JGR Space Physics

RESEARCH ARTICLE
10.1029/2022JA030813

Key Points:

- The plasma response to large antenna emission amplitudes triggering non-linear plasma perturbations is simulated
- Ion dynamics contributions to large amplitude propagating electric signals in the plasma are crucial and therefore should not be neglected
- Mutual impedance diagnostic performances are acceptable for emission amplitudes corresponding to electric-to-kinetic energy ratios up to 0.1

Correspondence to:
L. Bucciantini,
luca.bucciantini@cnrs.fr

Citation:
Bucciantini, L., Henri, P., Wattieaux, G., Califano, F., Vallières, X., & Randriamboarison, O. (2022). In situ space plasma diagnostics with finite amplitude active electric experiments: Non-linear plasma effects and instrumental performance of mutual impedance experiments. *Journal of Geophysical Research: Space Physics*, *127*, e2022JA030813. https://doi.org/10.1029/2022JA030813

Received 1 JUL 2022
Accepted 23 NOV 2022

In Situ Space Plasma Diagnostics With Finite Amplitude Active Electric Experiments: Non-Linear Plasma Effects and Instrumental Performance of Mutual Impedance Experiments

L. Bucciantini[1], P. Henri[1,2], G. Wattieaux[3], F. Califano[4], X. Vallières[1], and O. Randriamboarison[1]

[1]Laboratoire de Physique et Chimie de l'Environnement et de l'Espace (LPC2E), CNRS, Université d'Orléans, Orléans, France, [2]Laboratoire Lagrange, OCA, UCA, CNRS, Nice, France, [3]Laboratoire Plasma et Conversion d'Energie (LAPLACE), CNRS, Université de Toulouse, Toulouse, France, [4]Dipartimento di Fisica, Università di Pisa, Pisa, Italy

Abstract Mutual impedance (MI) experiments are a kind of plasma diagnostic techniques for the identification of the in situ plasma density and electron temperature. These plasma parameters are retrieved from MI spectra, obtained by perturbing the plasma using a set of electric emitting antennas and, simultaneously, retrieving using a set of electric receiving antennas the electric fluctuations generated in the plasma. Typical MI experiments suppose a linear plasma response to the electric excitation of the instrument. In the case of practical space applications, this assumption is often broken: low temperature plasmas, which are usually encountered in ionized planetary environments (e.g., RPC-MIP instrument onboard the Rosetta mission, RPWI/MIME experiment onboard the JUICE mission), force toward significant perturbations of the plasma dielectric. In this context, we investigate MI experiments relaxing, for the first time, the assumption of linear plasma perturbations: we quantify the impact of large antenna emission amplitudes on the (a) plasma density and (b) electron temperature diagnostic performance of MI instruments. We use electrostatic 1D-1 V full kinetic Vlasov-Poisson numerical simulations. First, we simulate the electric oscillations generated in the plasma by MI experiments. Second, we use typical MI data analysis techniques to compute the MI diagnostic performance in function of the emission amplitude and of the emitting-receiving antennas distance. We find the plasma density and electron temperature identification processes robust (i.e., relative errors below 5% and 20%, respectively) to large amplitude emissions for antenna emission amplitudes corresponding to electric-to-thermal energy ratios up to $\left(\epsilon_0 E^2\right)/(n_0 k_B T_e) = 0.1$.

1. Introduction

Mutual impedance (hereafter MI) experiments are a kind of in situ plasma diagnostic instruments that enable measurements of the absolute plasma density and the electron temperature through the dynamical response of a probed plasma to an external electrical excitation. Such measurement techniques were proven successful for several ionospheric (Bahnsen et al., 1988; Béghin & Debrie, 1972; Décréau et al., 1978; Grard, 1997; Pottelette et al., 1975; Pottelette & Storey, 1981; Storey et al., 1969) (e.g., ISOPROBE experiment onboard the AUREOL-3 satellite, for the ARCAD-3 mission, Béghin et al., 1982) and planetary space missions (e.g., the RPC-MIP instrument, J. Trotignon et al., 2007, onboard the ESA Rosetta mission). Different versions of MI experiments will also contribute to new exploratory missions such as the joint ESA-JAXA BepiColombo mission with the PWI/AM2P experiment (Kasaba et al., 2020; J. Trotignon et al., 2006), the JUICE ESA mission with the RPWI/MIME experiment and the Comet Interceptor ESA mission with the DFP-COMPLIMENT instrument (Snodgrass & Jones, 2019). New versions of MI experiments are currently being developed to adapt to the constraints of nano/microsatellite platforms.

The basic principle of MI experiments is the following. Plasma parameters such as the electron density and temperature are obtained through the analysis of the so-called MI spectrum. It is defined as the electrical impedance between an emitting and a receiving electric antenna embedded in the plasma to diagnosed (Storey et al., 1969; Chasseriaux et al., 1972; Béghin, 1995; Gilet et al., 2017; Wattieaux et al., 2019). Practically, the electron density and temperature are derived as follows. The plasma environment is perturbed by the emission of a succession of elementary electric sinusoidal oscillations injected in the plasma through the emitting electric antennas. Simultaneously, the electric oscillations that propagate in the probed plasma are measured with the receiving antennas. Such oscillations correspond to the plasma response at the emitted frequency. This frequency is modified step by step to cover a given range of frequencies and build up the MI spectrum. We hereafter refer to this process as

frequency sweep. The MI spectrum is a function of the plasma dielectric and it exhibits resonant signatures at the plasma characteristic frequencies (plasma eigenmodes). For instance, in the case of an unmagnetized plasma, MI spectra present one resonant signature at the plasma frequency. The electron density and the temperature are retrieved from the position and the shape of the resonance, respectively (Chasseriaux, 1972; Chassériaux, 1974).

The state-of-the-art methods used to model the instrumental response of MI experiments consider a variety of situations or processes known to significantly impact the instrumental response: (a) in collisionless plasmas, various types of distribution functions that account for different plasma populations (Gilet et al., 2017; Wattieaux et al., 2019), (b) the peculiar boundary conditions imposed by a conductive spacecraft carrying the experiment (Geiswiller et al., 2001), and (c) the influence of spacecraft charging that generates a plasma sheath surrounding the spacecraft and the instrument (Wattieaux et al., 2019). These models are all based on the assumption of a linear response of the plasma to the electric excitation of the instrument. This means that such models assume that the emitting antennas introduce small enough electric perturbations within the plasma, so that its dynamics is defined by its linear dielectric (Grard, 1969). Therefore, they assume negligible non-linear effects triggered by the emission process. Hence, they assume that the electric energy injected by the emitting antenna is much smaller than the thermal energy of the plasma to be diagnosed.

To ensure small perturbations of the plasma dielectric, MI experiments are designed to emit low amplitude signals. Practically, this is done by limiting the voltage imposed on the emitting antenna. This also has the advantage of limiting the electric power consumption required for MI space experiments.

However, the voltage imposed on the emitting antenna cannot be too small to ensure a satisfactory signal-to-noise ratio.

First, the amplitude of the received signal is proportional to that of the emitted signal. A large enough emitted signal therefore corresponds to an increased amplitude for the received signal. Strong emissions are particularly needed if the distance between emitting and receiving antenna is large. This is the case for MI instruments designed to probe hot space plasmas, for example, with particles energy of the order of 10 eV. For instance, the so-called LDL mode of the RPC-MIP instrument on Rosetta designed to observe hot plasmas near comet 67P/CG, the PWI/AM2P experiment on BepiColombo that will monitor hot plasmas in Mercury's environment and the RPWI/MIME experiment on JUICE that will investigate hot plasmas in the ionosphere of Ganymede.

Second, the instrument design must ensure that the received signal is above the instrumental noise. Instrumental noise is essentially composed of two main sources. On the one hand, the background noise of the instrument itself. On the other hand, the overall electrical noise generated by the platform and the rest of the payload. This second source is often referred to as the electromagnetic compatibility (EMC) of the spacecraft (ECSS-E-ST-20-07C handbook of ECSS, Youssef, 1996). EMC is costly for standard platforms and particularly delicate for nanosatellite platforms. Sufficiently large amplitude emission signals therefore mitigate the lack of EMC by improving the signal-to-noise ratio. It is therefore expected that large amplitude emissions might be preferable for future MI experiments designs, especially those dedicated to nanosatellite platforms.

On the one hand, from a practical point of view, there is therefore a net benefit in increasing the amplitude of the signal emitted in the plasma to increase the signal-to-noise ratio. On the other hand, from a plasma diagnostic point of view, there are net benefits in decreasing the amplitude of the signal emitted in the plasma. First, it ensures that the plasma response is described by its linear dielectric. Second, it limits the perturbations on other instruments of the payload such as interferences due to the MI emitted signal. All in all, a trade-off is chosen to ensure a large enough signal to be measured, for a small enough signal to be emitted: between few 10s mV and 1 V in typical space plasmas.

However, even with such trade-off, the linear plasma response hypothesis is often broken in ionized planetary environments, especially in dense, low-energy plasma regions. A recent example is given by the cold cometary plasma probed by Rosetta in the inner coma of comet 67P/CG, with electron temperatures as low as 0.1 eV independently measured by both the MI RPC-MIP (Wattieaux et al., 2020) and the Langmuir Probe RPC-LAP (Eriksson et al., 2017; Odelstad et al., 2020). Similar situations are also expected to be encountered by the RPWI/MIME experiment onboard JUICE in the ionosphere of Ganymede. In such cases, the thermal energy of the electrons can hardly be considered much larger than the injected electric perturbation. Hence, non-linear plasma effects (e.g., wave-wave and wave-particle interactions) are expected to strongly modify the plasma response to MI emissions. The assumption of a linear plasma dielectric response to the instrument perturbation becomes

invalid. Consequently, it is necessary to assess the plasma diagnostic performance of MI experiments in such common situations.

In this context, the objective of this study is to assess how strong the electric emissions can be in active in situ plasma measurements such as MI experiments, while preventing significant losses in instrumental performance. To this purpose, this study aims at relaxing, for the first time, the assumption of linear perturbations of the local plasma environment in MI instrumental modeling in order to investigate the influence of the plasma non-linear effects on the MI instrumental response. Practically, we aim at quantifying the impact of non-linear effects on MI diagnostics by assessing the error both in electron density and temperature measurements for large emission amplitudes.

The investigation described in this paper is performed by means of 1D-1 V full kinetic numerical simulations that model the plasma response to an external electric antenna, by solving the Vlasov-Poisson coupled equations for both ions and electrons.

This document is organized as follows. The numerical models adopted in this investigation are described in Section 2. The initialization of the numerical model and its validation are described in Appendix A and Appendix B, respectively. For repeatability purposes, the parameters defining the numerical simulations described in this study are listed in Appendix C. The non-linear effects generated in the plasma by strong electrical antenna excitations are described in Section 3, and their consequence on plasma diagnostics performed by MI experiments is quantified in Section 4. We conclude by discussing the implication for both past and current space mission data analysis, as well as for future instrumental designs in Section 5.

2. Model Description: 1D-1V Vlasov-Poisson

We consider a non magnetized, homogeneous, collisionless plasma composed of electrons and ions initially described by a single Maxwellian velocity distribution function. An electrical antenna is used to inject an external electric field perturbation to which the plasma reacts self-consistently. We neglect in our model the perturbations arising from the presence of the plasma sheath surrounding the antennas used for MI measurements.

The simulation models used in this study are based on the numerical integration of the Vlasov-Poisson system of equations that describe the spatio-temporal evolution of electron and ion distribution functions ($f_e(t,x,v_e)$ and $f_p(t,x,v_i)$, respectively, where t is the time, x the position in the plasma and v the electrons and ions velocity). The numerical integration scheme is the one described by Mangeney et al. (2002). The Vlasov equation used to evolve in time the electron and ion distribution function, simplified considering a negligible magnetic field, reads:

$$\frac{\partial f_\gamma(x,t,v_\gamma)}{\partial t} + \vec{v_\gamma}\cdot\nabla f_\gamma(x,t,v_\gamma) + \frac{q_\gamma}{m_\gamma}\vec{E}\cdot\nabla_{\vec{v_\gamma}} f_\gamma(x,t,v_\gamma) = 0 \tag{1}$$

where $\gamma = e, i$ represents the species and E is the electric field.

We limit our study to the 1D-1V electrostatic case. We use the model previously used in Henri et al. (2010), modified adding multiple external emitting electric antennas modeled using oscillating charge densities in the Poisson equation:

$$\nabla\cdot\vec{E} = e\frac{n_i(x,t) - n_e(x,t)}{\epsilon_0} + \frac{\rho_{ext.}(x,t)}{\epsilon_0} \tag{2}$$

where n_e (resp. n_i) is the electron (resp. ion) density and $\rho_{ext.}$ the external charge density.

The equations are normalized using electron characteristic quantities: the elementary charge e, the electron mass m_e, the Debye length λ_D, the time ω_p^{-1}, with $\omega_p = \sqrt{(e^2 n_0)/(\epsilon_0 m_e)}$ the angular plasma frequency, and the mean density n_0. It follows that velocities are normalized by the electron thermal speed $v_{the} = \lambda_D\omega_p$, the electric field by $E = (m_e v_{the}\omega_p)/e$ and the charge density at the antenna by $\bar{\sigma} = en_0\lambda_D$.

The numerical simulations are performed using periodic boundary conditions in physical space and assuming electron and ion distribution functions equal to zero for velocities outside the given velocity range (i.e., $f_e(x, |v_e| > v_{e,\max}, t) = 0$ and $f_p(x, |v_i| > v_{i,\max}, t) = 0$). Tables C1 and C2 list the simulation parameters.

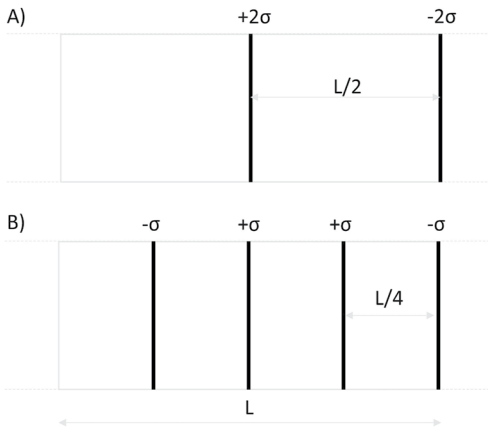

Figure 1. Representation of the emitting antennas configuration in the periodic simulation box. The top (resp. bottom) panel represents the model A (resp. B), characterized by two (resp. four) emitting antennas.

The simulations are initialized with uniform single Maxwellian distribution functions for ions and shifted Maxwellian distribution functions for the electrons to minimize transient effects. Such initialization is discussed in Appendix A. Transient signals will be investigated in a future dedicated work and are out of the scope of this study.

Each emitting antenna is modeled as the external source $\rho_{ext.}(x, t) = \sigma(t)\delta(x)$ characterized by the following oscillating charge term:

$$\sigma(t) = \sigma_0 \sin(\omega t) \tag{3}$$

where σ is the oscillating charge per unit surface, σ_0 is the amplitude of the oscillating charge, $\omega = 2\pi f$ is the angular frequency with f the emission frequency. Each of our 1D antennas is equivalent in 3D space to an oscillating, uniformly charged, infinite planar grid. Such a grid is supposed to be so thin that the collection of particles at its surface is negligible, resulting in particles moving freely across the antennas. This choice, also adopted in previous studies (Buckley, 1968), allows one to neglect the collection of electrons and ions from the emitting antenna. Each external antenna generates an oscillating electric signal composed of one uniform term (hereafter called far-field term) and a spatially damped term that propagates to the surrounding plasma from the position of the antenna (hereafter called close-field term) (Podesta, 2005). The far-field term corresponds to the electric field expected for the cold plasma limit (Chasseriaux et al., 1972) (i.e., $\omega \gg \omega_p$), while the close-field term represents the wave-component of the perturbation generated by the emitting antennas. Periodic boundary conditions on the simulation box require the use of, at least, two antennas of opposite oscillating charges. This configuration is equivalent to that of an oscillating capacitor, composed of two parallel infinite charged planes embedded in the plasma. Such capacitor perturbs the surrounding plasma with an electric field that is the sum of (a) a spatially constant far-field term and (b) close-field terms propagating in-between the two electrodes.

In our 1D model, the far-field term is equivalent, in 3D, to the electric field component that would decrease in $d_{ph.}^{-2}$ with the distance, $d_{ph.}$, from a point source emitting antenna. The close-field term is equivalent in 3D to the radial component of the wave that would propagate from the same emitting point source antenna to the surrounding plasma. We note that in 1D the amplitude of the electric field oscillations at large distances from the emitting antennas is overestimated w.r.t. that expected in 3D due to the far-field term. In order to account for this 1D artifact, we use in our study two different antennas configurations, hereafter called model A and model B (top and bottom panel of Figure 1).

Model A is optimized for the investigation of the non-linear effects triggered in the plasma by the MI emission signal. In particular, it benefits from the presence of the 1D artifact term: enhanced electric field fluctuation amplitudes correspond to enhanced growth-rate of the generated non-linear plasma perturbations. Thus, the simulation durations needed to study non-linear plasma perturbations are reduced. For this model, the positions of the emitting capacitors plates are chosen in order to maximize the distance between any two opposite charge electrodes. Practically, this is done by imposing the distance between the electrodes (represented as vertical lines in top panel of Figure 1) of each capacitor as half the length of the numerical spatial box and by superposing, for any two neighboring capacitors, the antennas that emit the same electric signal.

Model B is optimized for the quantitative investigation of MI diagnostic performance. It is devised to obtain MI spectra that either consider or neglect the effects of the 1D artifact depending on the position in the simulation box at which the electric fluctuations are retrieved. We consider (resp. neglect) the effects of the 1D electric-field artifact term by analyzing the electric oscillations generated in the plasma between two opposite (resp. same) charge antennas, where the far-field component is doubled (resp. canceled out). The positions of the antennas in the numerical box are chosen to maximize both the distance between neighboring capacitors and the distance between the plates of each capacitor. Practically, for this model, any two emitting antennas are separated by a distance equal to a quarter of the numerical spatial box length. This model allows one to investigate what non-linear effects are triggered by the close-field and far-field terms separately.

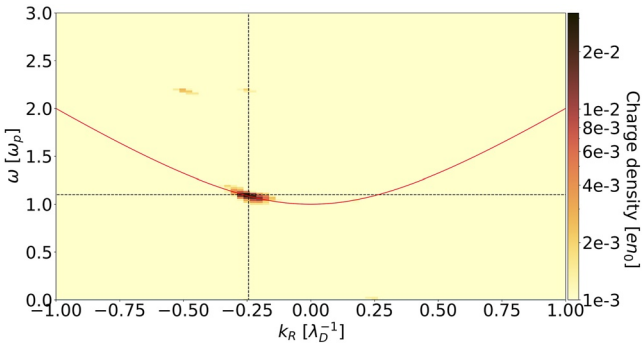

Figure 2. Charge density Fourier spectrum, in the real wavenumber-frequency space (k_R, ω), for simulation NF_01. The horizontal and vertical dotted black lines indicate the Langmuir wave at the antenna emission frequency ($-k_L$, ω_L). The Langmuir wave dispersion relation is shown as a red solid line.

Since the contribution of the far-field term is always present in 3D experimental MI spectra, for consistency with 3D MI experimental measurements, in this document we only discuss the plasma density and electron temperature obtained *including* such contribution. In the following, the plasma density and the electron temperature are obtained by applying the same data analysis techniques used for the investigation of experimental MI spectra (Gilet et al., 2017; Wattieaux et al., 2020).

3. Non-Linear Effects Generated in an Unmagnetized Space Plasma Excited by an External Large Amplitude Oscillating Antenna

In this section, we investigate the impact of moderate to strong electric antenna emission at a given frequency on the nearby perturbed plasma.

We define the electric-to-thermal energy ratio $\alpha = (E^2\epsilon_0)/(n_0 k_b T_e)$ as the parameter identifying the level of non-linearity associated to the electric field E, driven by the antenna emission. This ratio depends on the amplitude and on the frequency of the oscillating electric potential at the antenna. In particular, the electric field that propagates in the plasma scales with frequency ω as the inverse of the collisionless unmagnetized cold plasma dielectric permittivity, corresponding to $\left(1-\omega_p^2/\omega^2\right)^{-1}$ (Podesta, 2005) for $\omega \geq \omega_p$. In order to model different levels of α that can be achieved in MI experiments, we compare a number of simulations made using different frequencies but with same emission amplitudes.

The numerical simulations are set on the typical timescale of experimental MI emission durations, which turns out to be of the order of $N = 15$ oscillation periods of the emitted frequency. As a consequence, we neglect all effects that would develop over larger timescales. The total simulation time, the size of the physical box, the velocity range over which the ion and electron distribution functions are defined, as well as all other most relevant parameters are listed in Table C1.

In the following, we investigate with Model A (a) the non-linear perturbations triggered by single frequency emissions with a fixed ion background (Section 3.1) and (b) the impact of the ion dynamics on the perturbation evolution (Section 3.2).

3.1. Large Amplitude Perturbations of the Plasma Dielectric With Fixed Ions

In this section we consider the case of a fixed neutralizing background of ions and focus on the electron dynamics only. In particular, we investigate the plasma response to electric signals generated by an oscillating charge with amplitude $\sigma = 0.1\bar{\sigma}$ at three different frequencies: $0.5\omega_p$ (simulation NF_01), $1.1\omega_p$ (simulation NF_02) or $2.0\omega_p$ (simulation NF_03). The corresponding electric-to-thermal energy ratios are: 0.01, 0.33, 0.01.

On the one hand, for antenna emissions at $0.5\omega_p$ and $2.0\omega_p$, the electric perturbation that propagates in the plasma oscillates at the emission frequency. However, the perturbation is limited to regions close to the antennas, because it corresponds either to an evanescent wave (for $0.5\omega_p$) or to a propagating wave affected by strong Landau damping (for $2.0\omega_p$) (Brunetti et al., 2000) as consistent with a linear plasma response. In both cases, we do not observe any non-linear effect.

On the other hand, at frequency $\omega = 1.1\omega_p$ corresponding to wavenumber $k_L = -0.244\ \lambda_D^{-1}$, a non-linear plasma response occurs because of the conversion efficiency nearby the plasma frequency. The signature of this wave-wave interaction is shown in the charge density Fourier spectrum in Figure 2, where the black dashed lines indicate the emitted Langmuir wave at (k_L, ω_L) and the red line indicates the dispersion relation of Langmuir waves $\omega_L^2/\omega_p^2 = 1 + 3\lambda_D^2 k_L^2$.

First, on top of the emitted Langmuir wave, we also observe the so-called virtual wave at (2 k_L, 2 ω_L) (Dysthe & Franklin, 1970) which is represented as a localized increase in charge density at position ($k_R = -0.488\ \lambda_D^{-1}$, $\omega = 2.2\ \omega_p$) of Figure 2. Second, signatures of wave-particle interactions are observed. At the early stage of the

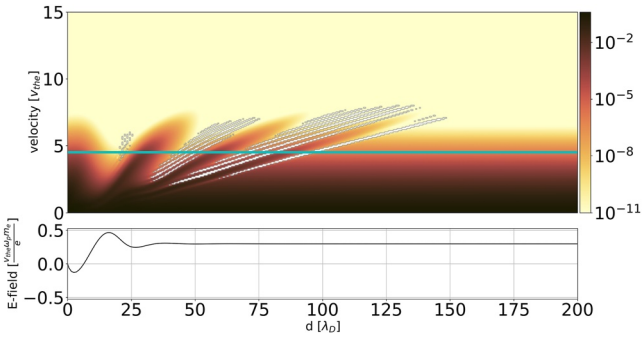

Figure 3. Efficient acceleration of electrons in regions close to the emitting antenna. Top panel: electron velocity distribution function in phase space; the blue line represents the phase velocity of the emitted Langmuir wave, for simulation NF_02 (emission frequency $\omega = 1.1\omega_p$) at time $t \simeq 20\omega_p^{-1}$. Bottom panel: corresponding electric field in the plasma, as a function of distance d from the emitting antenna, located at $d = 0$.

simulations $\left(t \simeq 20\omega_p^{-1}\right)$ we observe an efficient acceleration of the electrons pushed by the wave electric field and eventually propagating ballistically. In the (x, v_x) phase space domain, this process corresponds to the formation of finger-like filaments on the distribution function, as shown for the electron distribution function represented in top panel of Figure 3 between $v_e = 2v_{the}$ and $v_e = 7v_{the}$, at positions $[20\lambda_D{-}50\lambda_D]$, $[30\lambda_D{-}90\lambda_D]$, and $[50\lambda_D{-}130\lambda_D]$. We note that given the Langmuir wave packet propagating at group velocity $v_g = 0.67v_{the}$, the distance covered by the emitted wave packet in the plasma at $t \simeq 20\omega_p^{-1}$ is about $13\lambda_D$. At a later stage of the simulations $\left(t \simeq 120\omega_p^{-1}\right)$, the resonant electrons moving at nearly the phase velocity of the wave have been eventually trapped by the wave potential. This process leads to the formation of vortex-like structures in phase space. Such structures are visible in Figure 4 top panel at velocities near $v_\phi \simeq 4.5v_{the}$ which is the phase velocity of the emitted wave. We note that the Landau damping of the wave-packet does not affect the growth time rate of this trapping process, because the perturbing signal is *continuously* excited by the antenna emission. The oscillation period of these trapped electrons is $T_B = \sqrt{m_e/(eEk)}$ (O'Neil, 1965; Zakharov & Karpman, 1963). As expected, the trapping process starts nearby the emitting antenna, leading to nearly formed vortexes in phase space when the wave-packet propagating in the plasma reaches distance $L_v \simeq T_B v_\phi$. As the wave packet moves at group velocity v_g, no trapping is expected on timescales smaller than an *efficient* trapping time $t_{trap} \simeq L_v/v_g = T_B v_\phi/v_g = T_B\left(1 - \omega_p^2/\omega^2\right)^{-1} \gg T_B$. In the numerical experiment described in this section, we find $T_B \simeq 17\omega_p^{-1}$, for which vortexes in phase space form at a distance $L_v \simeq 75\lambda_D$ from the emitting antenna, starting from the *efficient* trapping time $t_{trap} \geq 113\omega_p^{-1}$. The above analysis is strongly limited by the fixed ions assumption to times shorter than the ion inertial time ($\sim m_i/m_e$ in dimensionless units) (Califano et al., 2007). This assumption is relaxed in the next section.

3.2. Large Amplitude Perturbations of the Plasma Dielectric for Moving Ions

In this section, we investigate the influence of the ion dynamics on the propagation of an antenna emitted oscillating electric potential by adding the ion Vlasov equation to the previous electron Vlasov-Poisson system (Equations 1 and 2). We use an ion-to-electron mass ratio $m_i/m_e = 100$ and an ion-to-electron temperature ratio $T_i/T_e = 0.1$. We consider a reduced mass ratio for computational reasons, while the temperature ratio is chosen to enable ion acoustic fluctuations to propagate.

We initialize the simulations with the same setup as in the fixed background limit discussed in Section 3.1. The investigated emission frequencies are $0.5\omega_p$ (simulation NI_01), $1.1\omega_p$ (simulation NI_02) and $2.0\omega_p$ (simulation NI_03), emission amplitude fixed to $\sigma = 0.1\ en_0\lambda_D$. The corresponding electric-to-thermal energy ratio in the plasma is 0.01, 0.33, and 0.01, respectively.

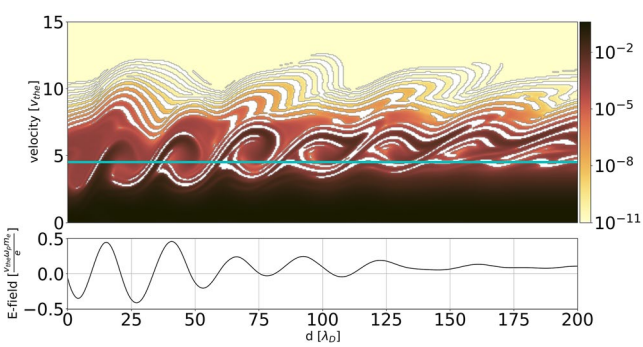

Figure 4. Signatures of particles trapping in phase space. Same as Figure 3 at time $t \simeq 120\omega_p^{-1}$.

At the emission frequencies of $0.5\omega_p$ and $2.0\omega_p$, the ion dynamics does not modify the propagation of the electric field in the plasma, as expected since no non-linear perturbations are observed (Section 3.1). The results (not shown here) are identical to those reported with fixed ions.

On the contrary, at emission frequency $\omega = 1.1\omega_p$, the ion dynamics strongly impacts the electric fluctuation propagating as a Langmuir wave at frequency $\omega_L = \omega$. Similarly to the model with fixed ions, we observe (a) ballistic electrons initially accelerated by the electric field escaping the wave packet, (b) wave-particle interaction signatures as phase space vortexes at the phase velocity of the emitted wave, (c) so-called virtual waves excited at $(-2k_L, 2\omega_L)$. On top of this, we also observe new signatures associated to the ion motion. Such signatures are shown in the ion (resp. charge) density Fourier spectrum in the bottom (resp. top) panel of Figure 5.

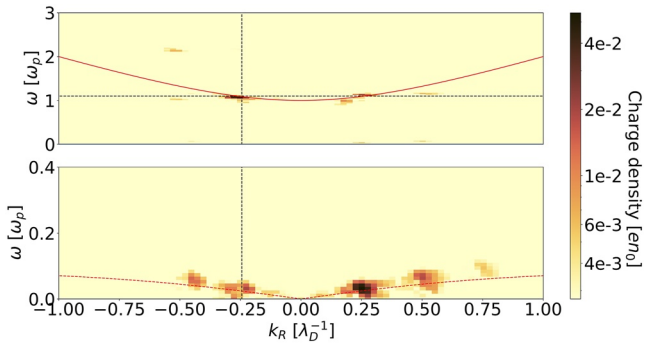

Figure 5. Charge and ion density Fourier spectra. Both top and bottom panel refer to simulation NI_02 (emission frequency $\omega = 1.1\omega_p$). Top panel: 2D Fourier transform of the net charge density, up to time $550\omega_p^{-1}$. The red solid line represents the Langmuir waves dispersion relation. The black dotted lines represent the ω_L and k_L of the emitted plasma wave. Bottom panel: 2D Fourier transform of the ion density, up to time $550\omega_p^{-1}$. The red dotted line represents the IAW waves dispersion relation. The black dotted line represents the k_L of the emitted plasma wave.

First, ion density oscillations show that ions are accelerated at the wavefront of the propagating Langmuir wave packet, resulting in the generation of ion acoustic oscillations propagating both forward and backward w.r.t. the Langmuir wave packet front (not shown here). The signature corresponding to these ion acoustic waves (IAW) is observed at ($\pm k_L$, ω_{IAW}) in the Fourier space of the ion charge density (bottom panel of Figure 5), where $k_L = 0.244\lambda_D$ is the wavenumber of the excited Langmuir wave and $\omega_{IAW} = 0.025\omega_p$ is the corresponding IAW oscillation frequency. Such frequency is obtained from the IAW dispersion relation $\omega_{IAW}^2 = \left(k_{IAW}^2 C_s^2\right)/\left(1 + k_{IAW}^2 \lambda_D^2\right)$ with C_s the ion sound-speed. Note that these ion acoustic modes do not correspond to what one would expect in the case of parametric excitation processes. In that case, as three waves interaction processes are triggered, the energy of the emitted Langmuir wave ($k_L = -0.244\lambda_D^{-1}$, $\omega_L = 1.1\omega_p$) would excite wave pairs respecting the resonant relations (Dysthe & Franklin, 1970) $\omega_L = \omega_1 + \omega_2$ and $k_L = k_1 + k_2$, where (k_1, ω_1) and (k_2, ω_2) are modes of the system. The generation of these ion acoustic perturbations is attributed to the ponderomotive force (Califano & Lontano, 1999; Henri et al., 2011) triggered by the strong electric energy gradient at the front of the Langmuir wave packet that acts as an equivalent pressure gradient on the ions. By performing a series of secondary simulations with larger ion-to-electron temperature ratios (i.e., $T_i/T_e \simeq 1$), we observed that such IAWs vanish directly after being generated at the wavefront of the propagating Langmuir wave due to their significant damping rate.

Second, large ion acoustic density oscillations $\Delta n_i/n_i$ reflect the emitted forward Langmuir wave ($-k_L = -0.244\lambda_D^{-1}$, $\omega_L = 1.1\omega_p$) into a backward Langmuir wave ($k_L = 0.244\ \lambda_D^{-1}$, $\omega_L = 1.1\ \omega_p$) (Tkachenko et al., 2021). This effect is equivalent to the ionospheric reflection of radio waves. With an emission frequency $\omega = 1.1\omega_p$, the Langmuir wave reflection occurs only in regions where ion density oscillations exceed $\Delta n_i/n_i > 0.2$, as confirmed by our simulations. Third, non-linear beats of the IAW at ($\pm\ k_L = \pm 0.244\lambda_D^{-1}$, $\omega_{IAW} = 0.025\omega_p$) trigger ion oscillations at the harmonic ($\pm\ 2k_L = \pm 0.488\lambda_D^{-1}$, $2\omega_{IAW} = 0.05\omega_p$), corresponding to the signature of localized charge density observed at that position in bottom panel of Figure 5. At later stages of the simulations, IAWs at the second harmonic ($3k_L$, $3\omega_{IAW}$) resulting from the non-linear interaction between (k_L, ω_{IAW}) and ($2k_L$, $2\omega_{IAW}$) are also observed in ion density oscillations (Figure 5, bottom panel). On top of that, virtual waves are observed at ($2k_L$, $\omega + \omega_{IAW}$) (Figure 5, top panel) as a result of the interaction between (k_L, ω) and (k_L, ω_{IAW}). The non-linear interactions described in this section have been identified in three steps. First, we investigated the time evolution of the energy location within the frequency-wavenumber domain. Second, we identified the resonant relations between wave triads. Third, we isolated the wave packets associated to each resonant mode by filtering them in Fourier space. Practically, this consists of isolating within the frequency-wavenumber domain each mode of interest and converting it back to time-space domain. By doing so, we have identified the location of the wave packets in physical space and confirmed at which time and location each identified three-wave interaction occurred. In this analysis, we have concentrated on three-wave interactions, associated to quadratic interactions, that is, the lower-order non-linear interactions in this model. We have also verified that higher order non-linear interactions are negligible in our simulations.

We conclude this section by emphasizing the necessity to self-consistently model the coupled electron and ion dynamics. This is particularly needed when targeting finite amplitude plasma oscillations at frequencies close to the plasma frequency, for which plasma non-linearities triggered by significant electric-to-thermal energy ratios come into play. Our simulations show that neglecting the ion motion results to a significant underestimation of the non-linear plasma interactions triggered by the instrument. When the ion motion is also modeled, IAWs can be triggered. This opens new channels for energy transfer from the emission frequency toward other frequencies, with an energy transfer that depends on both the emission frequency and the emission duration. This points out the need to self-consistently model both the electron and the ion dynamics when addressing the modeling and diagnostic performance of large MI emission amplitude likely to trigger non-linear plasma dynamics.

4. Significance for In Situ Density and Temperature Diagnostics Performed in Space Plasmas by Mutual Impedance Experiments

In this section, we quantify the consequences of the non-linear dynamics described in the previous Section 3 on the instrumental performance of MI experiments in space plasma diagnostics, focusing on in situ plasma density and electron temperature measurements. This objective is achieved by comparing and analyzing MI spectra modeled for both linear or non-linear responses of the diagnosed plasma. For this purpose, we simulate MI spectra obtained for electric antenna emissions ranging over electric-to-thermal energy ratio from 10^{-10} to 1. Note that we hereby define the electric-to-thermal energy ratio corresponding to each MI spectra as the energy ratio obtained for emission frequencies $\omega \gg \omega_p$. This choice is made to avoid any confusion associated to the frequency dependency of the electric potential oscillations in the plasma, during a MI frequency sweep, previously discussed in Section 3. In our analysis, we include the ions' dynamics, using an ion-to-electron mass ratio $m_i/m_e = 100$ (discussed in Section 4.5) and an ion-to-electron temperature ratio $T_i/T_e = 0.1$.

Note that the MI diagnostic technique used in experimental space applications is based on retrieving plasma parameters, such as the plasma density and electron temperature, from the shape of the MI spectra because it itself strongly depends on the *linear* plasma dielectric. This instrumental technique is therefore essentially based on the assumption of a *linear* response of the diagnosed plasma to the emitted electric perturbation. Practically, a linear plasma behavior is assumed when deriving plasma parameters using the MI diagnostic technique. From an instrumental point of view, whatever *non-linear* effect resulting from this emitted electric perturbation which would impact the shape of the MI spectra is therefore to be considered as spurious. Small perturbations of the plasma dielectric (i.e., a *quasi-linear* response of the diagnosed plasma) might be acceptable, from an instrumental point of view, as long as the resulting MI spectra does not differ much from the one expected in a linear case. For the above-mentioned reason, we also consider in this study a linear plasma response to the MI external electric excitation, in order to mimic typical experimental MI data analysis dedicated to the determination of both the plasma density and electron temperature. A linear plasma response is always assumed, even for plasma oscillations generated from significant antenna emission amplitudes for which *non-linear* perturbations of the plasma are occurring. The consequences of these *non-linear* plasma perturbations on the MI spectra might lead to a discrepancy between the *apparent* plasma density and electron temperature and the *actual* density and temperature. From the discrepancy between the *apparent* and the *actual* plasma parameters, we compute a diagnostic error, from which we derive the performance and robustness of the MI measurement technique. In particular, with this approach, we assess quantitatively the errors made in typical MI experiments when using data treatment techniques conceived for *linear* plasma perturbations to analyze MI spectra obtained for a *non-linear* plasma response.

4.1. Synthetic Mutual Impedance Spectra

MI spectra are built from the plasma response to MI emissions. A MI emitting electric antenna with oscillating electric signals of known amplitude A and frequency ω perturbs the plasma. *Simultaneously*, receiving electric antennas measure the electric potential fluctuations that have propagated in the diagnosed plasma, at the same frequency ω. The total duration of the emission signal is $t_\omega = NT_\omega$, where $T_\omega = 2\pi/\omega$ is the oscillation period and the amount of repetitions is chosen $N = 15$ in this work. This choice is consistent with the typical instrumental design of MI instruments. Practically, MI experiments successively scan one frequency after the other within a predefined frequency range of interest, to perform a MI frequency sweep. In our numerical experiments, we however choose to perform separate simulations for each emitted frequency. Therefore, we neglect any possible coupling between what would be successive emitted frequencies of a MI frequency sweep. In doing so, we assume that the waiting time between two successive emissions is sufficient for the plasma to relax back to its unperturbed state. This choice is discussed in Section 4.4.

Mimicking experimental MI applications, we investigate MI frequency sweeps characterized by a relative frequency resolution $\Delta\omega/\omega = 5\%$, that corresponds to a relative density resolution of $\Delta n_e/n_e = 10\%$. Such resolution is consistent with that used in recent MI experiments, such as the DFP-COMPLIMENT experiment of the ESA Comet Interceptor mission. This investigation is performed using model B, considering the contribution of the far-field term (described in Section 2). The list of settings parameter defining the simulations from which MI spectra are built is shown in Table C2.

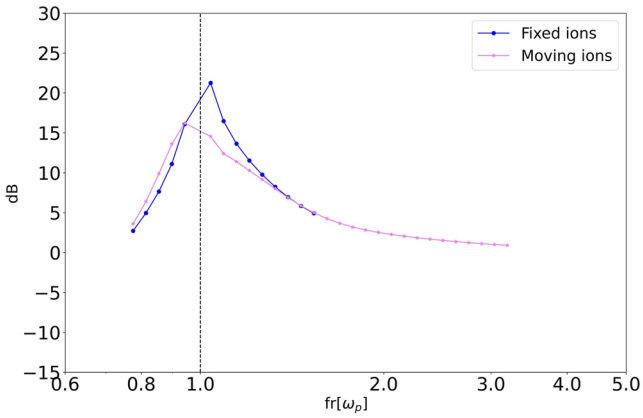

Figure 6. Mutual impedance spectra obtain with immobile (blue) and mobile (violet) ions. Both spectra are obtained for $\alpha = 0.6$ at distance $d = 5\lambda_D$ from the emitting antenna.

Using a dipolar reception antenna configuration, MI spectra are built from the electric potential oscillation difference measured between two electric antennas located at distance d and $2d$ from the emitting antenna, with d ranging from $5\lambda_D$ to $40\lambda_D$. These distances between the emission and reception antennas correspond to the typical MI experiment emitting-receiving antennas distances in previous and forthcoming space missions (Rosetta RPC-MIP, BepiColombo PWI/AM2P, JUICE RPWI/MIME, Comet Interceptor DFP-COMPLIMENT).

From the electric potential oscillations obtained in our numerical simulations, synthetic MI spectra are built using the following procedure.

1. First, we apply signal apodization to the electric potential oscillations. In this study, we adopted the Hann window, the same apodization technique currently adopted for the on-board analysis of MI measurements in previous space applications, such as RPC-MIP on Rosetta, AM2P on BepiColombo, and MIME on JUICE.
2. Second, we compute, at the emission frequency ω, the amplitude of the signal from a Discrete Fourier Transform of this windowed time series. We repeat this process for each emitted single frequency to obtain a spectrum.
3. Third, the obtained spectrum is normalized by the offset introduced by the Hann window, in order to correct for the apodization.
4. Finally, the resulting spectrum is normalized by the corresponding MI spectrum obtained in vacuum, a procedure usually performed with MI experiments (Henri et al., 2017). Indeed, under a linear plasma response assumption, this normalized MI spectrum is independent of the antenna emission amplitude. Therefore, this normalization procedure ensures an unbiased comparison between spectra obtained for different electric-to-thermal energy ratios. The resulting normalized MI spectrum is expressed in decibel scale, where the reference amplitude is that obtained for vacuum conditions.

For this investigation, we assume negligible perturbations of MI spectra related to noise. This assumption is not valid for experimental space applications, where the influence of *instrumental noise* on MI measurements is, at times, significant. The *instrumental noise*, related to the electronics of the MI instrument, affects the accuracy of the measurements. Typically, it affects experimental MI spectra with perturbations of the order of 1 dB and therefore, in order to mimic MI experimental space applications, we discard all perturbations of MI spectra up to 1 dB.

We have shown in Sections 3.1 and 3.2 that it is necessary to model both the electron and ion dynamics when investigating the propagation and evolution of finite amplitude waves associated to large amplitude emissions. We now illustrate (Figure 6) to what extent discarding the ion dynamics impacts MI measurements. We compare two MI spectra obtained either modeling (violet line) or neglecting (blue line) the motion of ions. Both spectra are computed at distance $d = 5\lambda_D$ from the emitting antennas and $\alpha = 0.6$ for which significant non-linear plasma interactions are expected. We note that the contribution of the ion dynamics significantly modifies the resonant shape of the spectra. In particular, we find differences up to 7 dB, which is well above the typical instrumental noise of MI measurements.

Therefore, in the rest of this work, we shall only consider numerical simulations that include both the electron and ion dynamics when investigating MI spectra. We now concentrate on the impact of finite amplitude emissions on MI spectra.

Examples of synthetic MI spectra are shown in Figure 7, for different electric-to-thermal energy ratios, for the emitting-receiving antennas distances $d \simeq 5\lambda_D$, $d \simeq 10\lambda_D$ and $d \simeq 20\lambda_D$, from top to bottom panels.

On the one hand, we observe that the MI synthetic spectra obtained for electric-to-thermal energy ratios $\alpha \leq 10^{-2}$ (corresponding to simulations SI1_01 to SI1_14) and represented as a light blue line are essentially identical (within the typical *instrumental noise* levels) to the linear spectra (corresponding to simulations SL_01 to SL_48) obtained for $\alpha = 10^{-10}$ and represented as a blue line.

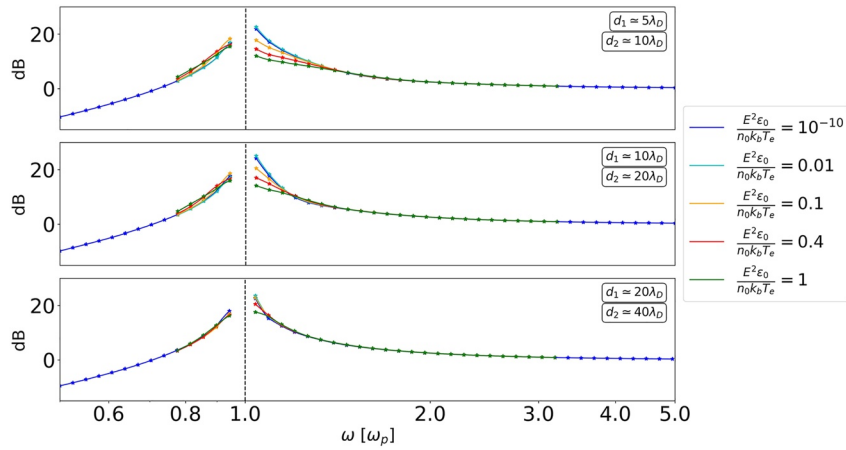

Figure 7. Mutual impedance spectra. The distances of the two receiving antennas from the emitting antenna are represented as d_1 and $d_2 = 2d_1$. From top to bottom panel, mutual impedance spectra are obtained for $d_1 \simeq 5\lambda_D$, $d_1 \simeq 10\lambda_D$, and $d_1 \simeq 20\lambda_D$, for different antenna emission amplitudes (solid lines).

On the other hand, when $\alpha > 10^{-2}$ (i.e., from simulations SI2_01 to SI2_14, SI3_01 to SI3_14, and SI4_01 to SI4_14), we observe instead significant differences between the associated spectra (i.e., orange, red, and green lines) and the reference spectra (blue line), especially at frequencies close to the plasma frequency for spectra obtained at $d \leq 20\lambda_D$. The discrepancies observed at frequencies close to the plasma frequency are consistent with the results of Section 3.2, where we have shown that the plasma is non-linearly perturbed by finite amplitude antenna emissions at frequency close to the plasma frequency ($\omega = 1.1\omega_p$). Note that, the discrepancies that we found exceeding typical *instrumental noise* levels are expected to be measurable in the case of experimental space applications for significant antenna emission amplitudes.

What is the expected trend of MI spectra disturbed by non-linear plasma perturbations induced by the finite amplitude antenna emission, compared to the undisturbed MI spectra associated to a linear plasma response?

The analysis performed in Section 3.2 suggests that the MI spectra, built from the electric oscillation measured in the plasma at the emission frequencies, should be affected by two counteracting phenomena, triggered by the finite amplitude antenna emission. On the one hand, non-linear wave-wave interactions open energy channels that redistribute the energy at frequencies different from the emission frequency. This results in a net *decrease* in the received (normalized) MI amplitude at the emission frequency, compared to the received (normalized) amplitude that would be measured in the linear case. On the other hand, wave-particle interactions also result in a non-linear feedback on the plasma distribution function (plateauing in velocity space) that decreases, or can even suppress, the spatial damping of the emitted wave packet. Note worthily, under a linear plasma response assumption, the MI spectra at frequencies above, and close to, the plasma frequency are strongly shaped by the spatial Landau damping of the Langmuir wave excited in the plasma by the emission antenna. Therefore, wave-particle interactions imply a net *increase* in the received (normalized) MI amplitude at the emission frequency, compared to the received (normalized) amplitude that would be measured in the linear case.

Because of these two counteracting phenomena, it is not straightforward to know the actual shape of the MI spectra close to the resonant frequency (in this study, the plasma frequency), hence the need for numerical simulations. For instance, in the specific conditions considered in this section (i.e., with antenna distances of $d \simeq 5\lambda_D$, $d \simeq 10\lambda_D$, and $d \simeq 20\lambda_D$), we find a maximum discrepancy between the MI synthetic spectra perturbed by non-linear plasma effects (e.g., green solid line in Figure 7) and the reference linear MI synthetic spectra (blue solid line in Figure 7) at the resonance peak of about 10 dB. This spectrally localized, but significant, discrepancy is well above the typical instrumental noise of MI instruments (e.g., 1 dB): we therefore expect such perturbations to actually be measurable, and possibly even dominant, for MI spectra obtained in low temperature space plasmas. It is therefore legitimate to assess quantitatively the impact of these "spurious" (from an instrumental diagnostic point of view) non-linear plasma perturbations of the MI spectra on plasma density and electron temperature measurements performance when using the MI diagnostic technique.

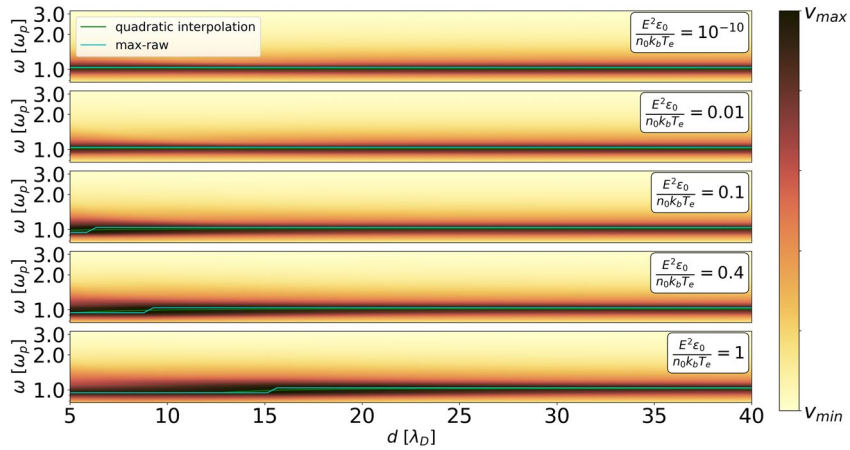

Figure 8. Mutual impedance dynamic spectra in function of the emitting-receiving antennas distance d. Each spectrum, normalized for the corresponding spectrum in vacuum, is represented between its minimum and maximum amplitudes. The plasma frequency is identified as the frequency of (a) the maximum of each spectrum (light blue line) and (b) the maximum of the quadratic interpolation of each spectrum (green line).

We describe in the following sections the procedure used to derive the plasma density (Section 4.2) and electron temperature (Section 4.3) from the normalized MI spectra, expressed in dB.

4.2. Plasma Density Diagnostic Performance for Strong Amplitude Emissions

We here focus on evaluating the plasma density diagnostic performance of MI experiments for finite amplitude antenna electric emissions likely to trigger non-linear effects in the diagnosed plasma. We do so in two steps. First, for each spectrum we estimate the plasma frequency (hereafter called *apparent* plasma frequency, $\omega_{p,app.}$). Second, we compute the plasma frequency relative error by comparing the apparent plasma frequency to the (known) *actual* plasma frequency (ω_p) of the spectrum as follows:

$$\frac{\Delta\omega_{p,app.}}{\omega_p} = \frac{\|\omega_{p,app.} - \omega_p\|}{\omega_p} \tag{4}$$

The MI plasma density diagnostic performance is then obtained by converting the plasma frequency relative error to plasma density relative error:

$$\frac{\Delta n_{e,app.}}{n_e} = \frac{\|n_{e,app.} - n_e\|}{n_e} = 2\frac{\Delta\omega_{p,app.}}{\omega_p}. \tag{5}$$

The considered frequency resolution of $\Delta\omega/\omega = 5\%$ corresponds to a plasma density resolution $\Delta n_e/n_e = 10\%$. We consider that MI experiment is robust against strong antenna amplitude emissions if the plasma density relative error is below this uncertainty.

We evaluate the plasma density diagnostic performance for antenna emission amplitudes corresponding to electric-to-thermal energy ratios $\alpha \in \left(10^{-10}, 1\right)$ (top to bottom panels of Figure 8), in function of the emitting-receiving antennas distance d ranging from $5\lambda_D$ to $40\lambda_D$.

The apparent plasma frequency is identified from MI spectra as the frequency corresponding to the position of the resonant peak signature in the spectra (Bahnsen et al., 1988; Béghin & Debrie, 1972; Décréau et al., 1978; Geiswiller et al., 2001; Gilet et al., 2017; Grard, 1997; Pottelette et al., 1975; Pottelette & Storey, 1981; Rooy et al., 1972; Storey et al., 1969). To account for the finite frequency resolution, we compute the apparent plasma frequency using three different methods. The first method consists of identifying the plasma frequency as the frequency corresponding to the maximum amplitude of the spectra (light blue line in Figure 8). This method is simple but with limited performances, since the difference between the *apparent* and *actual* plasma frequency is constrained by the discretization of the MI frequency sweep.

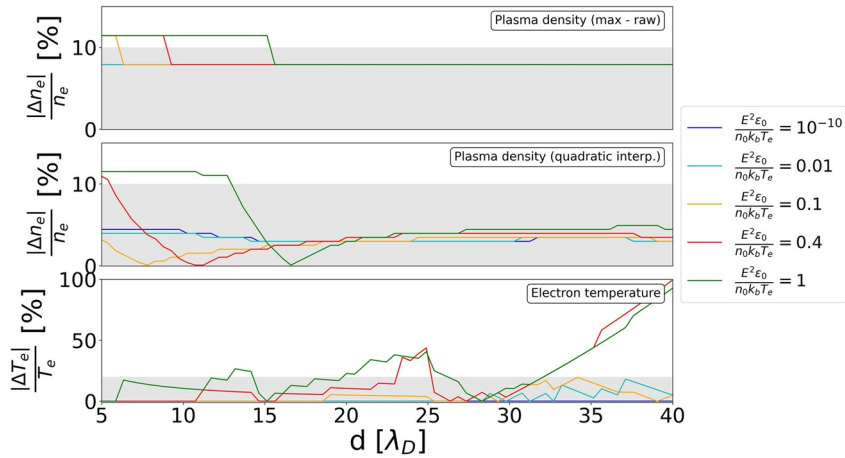

Figure 9. Mutual impedance plasma density and electron temperature diagnostic performance in function of the emitting-receiving antennas distance d. The diagnostic performance is obtained for electric-to-thermal energy ratios between 10^{-10} and 1 (solid lines). Plasma density resolution of 10% and electron temperature uncertainty of 20% represented as gray shaded areas. Plasma density relative errors obtained identifying the plasma frequency as the maximum of each spectrum (top panel) or the maximum of the quadratic interpolation of each spectrum (middle panel). Electron temperature relative error identified comparing the investigated spectra to reference spectra (bottom panel).

The second method consists of, first, interpolating the MI spectra using a polynomial interpolation of second order and, second, identifying the apparent plasma frequency as the frequency corresponding to the maximum amplitude of the interpolated spectra (green line in Figure 8). Using this method we mitigate the effect of the discretization in the MI frequency sweep.

The third method (not shown here) consists of, first, approximating the resonant peak signature of MI spectra using a Gaussian function and, second, identifying the apparent plasma frequency as the frequency corresponding to the maximum of such Gaussian function. Similarly to the second method, this method too is used to mitigate the effect of the discretization in the MI frequency sweep.

Apparent plasma frequencies derived using these methods are shown in Figure 8 in function of the distance from the emitting antennas, together with the MI spectra from which they are derived. The plasma density diagnostic performance of first and second method is shown in Figure 9 (top and middle panels, respectively).

Using this third method, the plasma density relative errors range between 6% and 50%. As they significantly exceed the uncertainty of 10%, our analysis indicates that the resonant peak of MI spectra is not well approximated by a Gaussian function and therefore this third method shall not be used for experimental applications.

For experimental space applications, we suggest the use of the second method (middle panel of Figure 9), for which the plasma density estimation errors, ranging between 0% and 12%, are minimized. The error on plasma density diagnostic due to plasma non-linearities remain below 5% (resp. 12%) for emission amplitudes corresponding to $\alpha < 0.1$ (resp. $\alpha = 1$). These errors are smaller than (resp. of the order of) the instrumental density resolution of 10% (gray shaded area in top and middle panels of Figure 9), associated to a frequency resolution of 5%. We conclude that the plasma density diagnostic performance of MI experiments is robust against the generation of non-linear plasma effects by strong antenna amplitude emissions.

4.3. Electron Temperature Diagnostic Performance for Strong Antenna Emission Amplitudes

We here focus on evaluating the electron temperature diagnostic performance and robustness of MI experiments when using finite amplitude antenna electric emissions, likely to trigger non-linear effects in the diagnosed plasma. We do so in three steps. First, we identify the apparent plasma density ($n_{e,app.}$) from MI spectra as described in the previous section. Second, we identify from the MI spectra the ratio between the (known)

emitting-receiving antennas distance and the (unknown) Debye length, hereafter called *apparent* Debye length $\lambda_{D,app.} = \sqrt{(\epsilon_0 k_B T_{e,app.})/(e^2 n_{e,app.})}$, from which the *apparent* temperature ($T_{e,app.}$) is obtained. Third, we evaluate the electron temperature diagnostic performance as the relative error between this *apparent* temperature and the *actual* (T_e) electron temperature we aim to measure.

$$\frac{\|\Delta T_{e,app.}\|}{T_e} = \frac{\|T_e - T_{e,app.}\|}{T_e} = \|1 - \frac{T_{e,app.}}{T_e}\| \tag{6}$$

This is done for the same emission amplitudes and emitting-receiving antennas distances as investigated in the previous section.

In previous space experiments, different techniques were used to derive the electron temperature from MI spectra in unmagnetized Maxwellian plasma. We hereafter recall three of those.

The first technique is based on identifying the frequencies at which anti-resonant signatures (i.e., local minima) are spotted on MI spectra (Geiswiller et al., 2001). Anti-resonances indicate that, for the corresponding frequencies, the wavelength of the wave emitted in the plasma is a multiple of the emitting-receiving antennas' distance d at which the MI spectrum is obtained. For anti-resonances to be spotted, the emitted electric fluctuations reaching the receiving antennas and used to build the spectra need to be composed of both the cold plasma electric field term (so-called far-field term) and the propagating wave term (so-called close-field term). Due to propagation effects, the close-field electric fluctuations, propagating in the plasma at group velocity, reach the positions of the receiving antennas after the delay time $t_{d.} = 2d/v_g$, where, for the anti-resonance to occur, d is expected to be a multiple of the wavelength of the emitted wave. For the emitted frequency ω, the delay time corresponds to $N_{d.} = t_{d.}/T$ repetitions of the oscillation period. Considering that the reception time period is synchronized to the emission, anti-resonances are expected to be spotted on the spectra if the delay time is negligible w.r.t. the total reception time period, corresponding to $N \gg N_{d.}$. For example, with a MI elementary sinusoidal signal emitted at $\omega = 1.1\omega_p$, the wavelength is $d \simeq 25.7\lambda_D$, the group velocity corresponds to $v_g = 0.67v_{the}$ and the delay amount of repetitions $N_{d.} \simeq 14$. Since in this study we focus on emission time periods corresponding to $N = 15$, anti-resonances are not expected to be spotted. As a consequence, this technique, designed for long emission durations, is discarded.

The second technique is based on the amplitude sharpness of the resonant peak of MI spectra (Chasseriaux et al., 1972; Décréau et al., 1978). This technique is also discarded here, since perturbations of MI spectra due to non-linear effects are enhanced at frequencies close to the plasma frequency (as found on Sections 3.2 and 4.1).

The third technique is based on a direct comparison between the experimental spectrum and different reference spectra (Wattieaux et al., 2020), which are theoretical spectra obtained assuming linear perturbations of the probed homogeneous plasma.

In our study, we use this third technique to identify the electron temperature associated to each *synthetic* MI spectrum.

We use as reference spectra those obtained for emission amplitudes corresponding to electric-to-thermal energy ratio $\alpha = 10^{-10}$, corresponding to a linear plasma response, that is, to negligible perturbations of the plasma dielectric. These reference spectra are obtained for emitting-receiving antennas distances $d_{f.}$.

To each *synthetic* spectrum, we associate a *reference* spectrum, hereafter called *matching* spectrum, defined as the one that minimizes the root mean squared error $\xi = \sqrt{\sum (x_i - y_i)^2 / L}$, where L is the amount of emitted frequencies for each spectrum, x_i and y_i are the Fourier components corresponding to the ith emitted frequency for the compared synthetic and reference spectra, respectively. To mimic typical experimental applications of this technique, the (known) actual plasma density of the reference spectra is imposed equal to the apparent plasma density of the synthetic spectrum (e.g., $n_{e,app.} = n_e$). As a consequence, this procedure is applied after the plasma frequency of the synthetic spectrum is identified following the procedure described in the previous section. From the emitting-receiving antennas distance corresponding to the matching spectrum, we estimate an apparent distance associated to the synthetic spectrum as $d_{app.} = d_{f.}$. Because of non-linear effects that might perturb the MI spectra, this apparent distance might differ from the actual distance d at which the synthetic spectrum

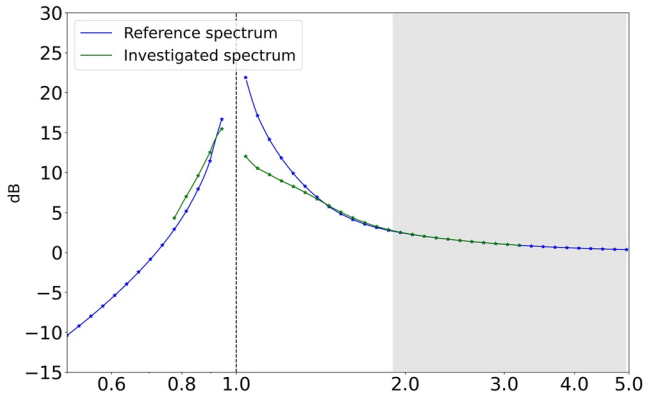

Figure 10. Illustration of the difference between the third technique and the improved third technique (gray region) for the identification of the electron temperature. Blue line represents the reference spectrum; green line represents the experimental (investigated) spectrum. The two spectra are computed for $\alpha = 10^{-10}$ and $\alpha = 1$ at distance $d = 5\lambda_D$. Using the third technique we compare the full spectra. Using the improved third technique we only compare the subpart of the spectra corresponding to the gray region.

is obtained. Both the apparent and actual distances correspond to the same *physical* distance:

$$d_{ph} = d_{app.}\lambda_{D,app.} = d\,\lambda_D \tag{7}$$

where d_{ph} is the (non-normalized) physical distance between emitting and receiving antennas, fixed by design of the MI instrument, $\lambda_{D,app.}$ the apparent Debye length and λ_D the actual Debye length. From the ratio between d and $d_{app.}$ we derive the electron temperature relative error as:

$$\frac{\|\Delta T_{e,app.}\|}{T_e} = \|1 - \frac{n_{e,app.}}{n_e}\left(\frac{d}{d_{app.}}\right)^2\| = \|1 - \left(\frac{d}{d_{app.}}\right)^2\| \tag{8}$$

In previous MI space applications, the uncertainty associated to this third technique was estimated of the order of 10%–30% (Décréau et al., 1978). In our study, in order to mimic experimental MI applications, we consider this technique robust against strong antenna emission amplitudes if the electron temperature relative error is below the threshold of 20%, hereby called *reference uncertainty*.

In our first attempt, we find significant electron temperature relative errors for the emission amplitude corresponding to the electric-to-thermal energy ratio of 1 (not shown here). These errors are above the reference uncertainty because in the comparison process is included also the resonant signature of MI spectra, for which enhanced perturbations are observed for strong emission amplitudes. Therefore, to improve the robustness of the process and reduce the electron temperature relative errors, we now modify the third technique by discarding the contribution of the resonant peak. We do so by filtering out, before the comparison, the Fourier components of MI spectra that correspond to frequencies below a given threshold frequency. In the range $1.0\omega_p$ to $2.0\omega_p$, the best electron temperature diagnostic performances are found for the threshold frequency of $1.9\omega_p$. The difference between the third technique and the improved third technique is illustrated in Figure 10. Using the third technique, the electron temperature is obtained by comparing one given experimental (investigated) spectrum (green line) to several different reference spectra (blue line). Using the improved third technique, the same comparison is performed but not using the full spectra: we use only a subpart of the spectra (i.e., the gray region) and discard the resonant peak, for which strong perturbations due to non-linear plasma interactions are expected.

Using this modified third technique, we find that for $\alpha = 1$ the electron temperature relative errors (green line in Figure 9 bottom panel) significantly exceed the expected temperature uncertainty (gray shaded area) for distances above $d \geq 34\lambda_D$. Since smaller α correspond to smaller electron temperature errors (as shown in Figure 9), a trade-off is required between (a) sufficiently strong emission amplitudes that ensure significant signal-to-noise ratios for MI measurements and (b) small temperature relative errors. Practically, we have identified the largest MI emission amplitude (colored lines in Figure 9) for which the electron temperature relative errors remain lower than the reference uncertainty (gray shaded area). In the investigated range of emitting-receiving antennas distances, we find that the maximum emission amplitude for which the electron temperature identification uncertainty is *always below* the reference uncertainty corresponds to $\alpha = 0.1$.

We conclude that, in 1D, the electron temperature identification process is affected by strong emission amplitudes. Small electron temperature diagnostic performance loss is ensured by perturbing the plasma with emission amplitudes corresponding to $\alpha \leq 0.1$. In Section 5, we discuss, on the basis of the results of our 1D investigation, what performances we expect for 3D MI experimental applications.

Our results suggest that only small modifications of the signatures of the normalized MI spectra are expected due to the excitation of non-linear effects. Therefore, in the case of experimental space applications, the use of an abacus of *reference* MI spectra might facilitate the identification process of the electron temperature. Note that this abacus should be derived for the particular MI experimental application of interest. In particular, it should consider both the specific geometric configuration of the spacecraft on which the instrument is mounted and the configuration of the MI instrument itself.

4.4. Diagnostic Impact of *Consecutive* Versus *Separate* Emission of Successive Frequencies

The MI emission signal is a composition of different elementary signals, each one corresponding to a different frequency. In the case of experimental MI space applications, MI spectra are built from the electric oscillations triggered in the plasma by the *consecutive* emission of all different elementary signals. In our investigation, instead, we simulate the perturbations of each elementary signal *separately*, performing different numerical simulations. In doing so, we *separate* the contributions of the different elementary signals and neglect any possible coupling between electric oscillations corresponding to different emitted frequencies. Practically, this corresponds to waiting for the plasma to regain its resting and unperturbed state between the emission of two successive elementary signals. While, for experimental space applications, this assumption is not always valid, in our investigation it is motivated by computational reasons. Indeed, the numerical investigation of the non-linear effects triggered by MI experiments requires a very large and detailed spatial domain. Such spatial domain coupled with a very fine velocity resolution mesh (mesh details given in Appendix C) results in unfeasible numerical simulations of the whole consecutive set of successive elementary signals.

Hereby, we quantify the error made when the coupling between plasma oscillations corresponding to the consecutive emission of different frequencies is neglected. To do so, we compare the MI spectra obtained from the (a) *separate* or (b) *consecutive* emission of given elementary signals. To this purpose, we build MI spectra, following the procedure described in Section 4.1, from the electric oscillations generated by the emission of elementary signals at frequencies $\omega_1 = 1.1\omega_p$, $\omega_2 = 1.32\omega_p$, and $\omega_3 = 1.584\omega_p$, for antenna emission amplitudes corresponding to electric-to-thermal energy ratios of $\alpha \simeq 10^{-10}$ and $\alpha \simeq 10^{-1}$. These frequencies are chosen because they discretize a large portion of the MI resonant peak signature, for which the perturbations due to finite antenna emission amplitudes are enhanced. For computational reasons, the perturbations are obtained for antenna emission amplitudes corresponding to an electric-to-thermal energy ratio up to $\alpha \simeq 10^{-1}$.

From the comparison between MI spectra obtained simulating (a) separately or (b) consecutively the emission of different elementary signals, we find a maximum discrepancy of about 2 dB. While this error exceeds the typical instrumental noise level of MI experimental space applications (which is also neglected), it still is of the same order. Due to such limited perturbations, we simplify the investigation and perform our numerical simulations by avoiding the consecutive emission of the different elementary signals.

4.5. Reduced Ion-To-Electron Mass Ratio and Limited MI Emission Time Period

In this section, we briefly discuss the choice of discarding representative ion-to-electron mass ratios like the proton-to-electron mass ratio $m_i/m_e \simeq 1{,}836$ in favor of the reduced mass ratio $m_i/m_e = 100$ for the investigation of MI diagnostic performance.

For experimental MI space applications, the amount of repetitions is typically chosen between $N = 10$ and $N = 100$ while in this analysis, for computational reasons, is set to $N = 15$. While the dependency of MI diagnostic performances on the amount of emitted repetitions, N, is outside the scope of this study, longer emission time periods indeed correspond to stronger non-linear perturbations of the plasma. In order to account for the selected limited amount of repetitions and investigate the perturbations of the MI diagnostic due to non-linear effects that would develop in the plasma for longer emission time periods, we choose to enhance the ion dynamics by increasing the ion acoustic frequency. In particular, for our investigation, we choose a reduced ion-to-electron mass ratio of $m_i/m_e = 100$ that enhances the ions' acoustic frequency by a factor ≥ 4.

5. Conclusions

MI instruments are in situ, active, electric experiments that provide plasma diagnostics, used to identify the plasma density and electron temperature in space plasmas. Such plasma parameters are derived from MI spectra which are obtained by actively perturbing the plasma to be diagnosed with a set of emitting antennas, while simultaneously retrieving the electric fluctuations generated in the same plasma. In practical instrumental design, the choice of the antenna emission amplitude is always the result of a trade-off. On the one hand, small antenna emission amplitudes ensure both small perturbations to other payload instruments and a linear plasma response. On the other hand, large emission amplitudes ensure signal-to-noise ratios suitable for both density and temperature identification. But, at the same time, they might trigger non-linear electric perturbations which could affect

the plasma diagnostic. In particular, diagnostic performance loss is expected when the electric energy of the emitted signal is large w.r.t. the electron thermal energy. In this study, for the first time, we relax in the modeling of MI experiments the hypothesis of a linear plasma response and investigate numerically the non-linear plasma perturbations on MI spectra generated by such experiments using the 1D-1V non-linear Vlasov-Poisson model.

We identify, for the first time, the maximum antenna emission amplitude that can be implemented to ensure robust and satisfactory diagnostic performances for both the plasma density and the electron temperature. In particular, we find that for antenna emission amplitudes corresponding to electric-to-thermal energy ratios up to 0.1 the relative errors on plasma density and electron temperature remain below 5% and 20%, respectively.

In situ space plasma observations performed in the solar wind by the STEREO spacecraft have shown that non-linear effects are present, in the range of frequency also used in MI experiments (i.e., close to the plasma frequency), for electric fluctuations of the plasma corresponding to electric-to-thermal energy ratios of $\alpha = 10^{-4}$ (Henri et al., 2011). For such energy ratios, our 1D numerical simulations show instead that negligible non-linear perturbations of MI spectra are expected. This means that, in the short MI emission duration, the growth time-rate associated to the non-linear effects triggered by such emission amplitude is not sufficient to develop perturbations that can significantly modify the spectra. Indeed, for larger antenna emission amplitudes the growth time-rate of the non-linear perturbations of the plasma is enhanced and modifications of the synthetic MI spectra are observed.

We note that our study suffers different limitations due to the numerical model we used. First, the use of our Vlasov-Poisson model prevented us from investigating emission amplitudes that corresponded to electric-to-thermal energy ratios significantly larger than 1, for which we found unstable numerical runs. Second, in our study the plasma nearby the antennas is assumed as homogeneous. In experimental space applications it is not the case, as plasma inhomogeneities (e.g., the antennas plasma sheath) envelope the antennas and affect the propagation of plasma waves. Dedicated studies will be performed in the near future to investigate how plasma inhomogeneities specifically affect MI measurements. Third, in our 1D description, the emitting antennas are modeled as infinite transparent plane grids. While the classic spherical or cylindrical shapes of MI antennas used for space application cannot be simulated, this choice enabled a significant simplification of the model. To investigate the impact of the antennas' shape on the MI measurements, models such as the DSCD model (Geiswiller et al., 2001; Wattieaux et al., 2019) could be used. However, these models are limited to the linear regime thus preventing the analysis in the presence of plasma non-linearities.

It is important to emphasize that our results overestimate the errors expected in the case of actual experimental measurements. Indeed, in our 1D numerical investigation, the electric field amplitudes remain mostly constant with the distance (far-field and close-field electric field components discussed in Section 2). Instead, in experimental 3D applications, the electric field oscillation amplitudes decrease with the distance from the emitting antennas in $1/d_{ph.}^2$, so that the electric-to-thermal energy ratio therefore decreases in $1/d_{ph.}^4$. Nevertheless our investigation represents the first step for the study of the non-linear plasma-antenna regime. For instance, let us consider a large amplitude MI emission ($\alpha = 1$) that triggers significant non-linear effects at a distance of 1 m from the emitting antennas. At a distance of 10 m, we expect significantly smaller non-linear perturbations as the electric field decreases by a factor 10^2 and α decreases by a factor 10^4. In other words, non-linear perturbation are likely to occur only in the vicinity of the emitting antenna. Thus, the maximum amplitude identified in this work (corresponding to $\alpha = 0.1$) is to be considered a conservative, lower value that ensures negligible plasma density and electron temperature identification errors. In order to go beyond this conservative maximum amplitude and account for both a fully realistic instrumental geometry and the associated spherical radial dependence of the potential, one would need to use a multidimensional (3D-3 V) Vlasov-Poisson model that would be extremely demanding computationally and out of reach of current supercomputers. This is out of the scope of this current paper but might be addressed in the future when computational resources allows it.

Part of the results found in our study are also applicable to another kind of active electric experiments dedicated to in situ space plasma diagnostics, namely, the so-called relaxation sounder experiments (hereafter called RS), such as the RS experiment(J. Trotignon et al., 1986) onboard the NASA ISEE spacecraft, the RS experiment(Harvey et al., 1979) onboard the ESA GEOS spacecraft, the wave experiment(Décréau et al., 1987) onboard the Swedish VIKING spacecraft, the RS experiment of the URAP instrument(Osherovich et al., 1993) onboard the NASA/ESA Ulysses spacecraft and the WHISPER experiment (Béghin et al., 2005; J. Trotignon et al., 2003; J. G. Trotignon et al., 2010) onboard the ESA CLUSTER spacecraft. RS are based on a measurement technique similar to that of MI experiments, with the main difference that emission and reception are not simultaneous.

For instance, in the case of the WHISPER instrument, emission occurs during 1 ms on a long-wire antenna while reception is performed on a double-sphere antenna a few ms later, measuring waves that are able to propagate near the characteristic frequencies of the plasma. This necessitates a relatively high amplitude excitation, corresponding to an excitation voltage greater than 50V. This emission amplitude is expected to trigger electric oscillations in the plasma with energy that strongly overcomes the thermal electron energy, therefore generating non-linear plasma perturbations. Combined with the large emitting-receiving antennas distance of such experiments (WHISPER antenna are 88 m in length), the high amplitude excitation allows the RS experiment probing a volume much larger w.r.t. the volume probed with MI experiments. On the one hand, non-linear effects are triggered by the large amplitude excitation. But, on the other hand, given the electric field amplitude decrease in distance as $1/d_{ph.}^2$, their influence is minimized in the overall response measured by the instrument. Moreover, considering the probed volume at play and also depending on the magnetospheric regions crossed by the CLUSTER satellite, plasma inhomogenities and non-Maxwellian electron distributions can be the main source of uncertainty. Several studies have been conducted to cross-validate simultaneous measurements from MI and RS instruments (Décréau et al. (1978) on GEOS, Béghin et al. (2005) on CLUSTER).

Our study provides guidelines for the choice of antenna emission amplitudes of experimental MI applications to ensure small non-linear perturbations of the plasma density and electron temperature diagnostic. Note that in our study we neglect all transient effects, which in the numerical simulations are damped by the chosen initialization of the model (Appendix A). The possible impact of transients on MI measurements diagnostic performance is left to future studies. Note also that these results should not concern double Maxwellian electron distribution functions, for which the MI resonance might appear at frequencies significantly below the plasma frequency.

Appendix A: Initialization of the Numerical Model

We hereby describe the initialization of the numerical simulations analyzed in this study. This initialization, based on the consistency between the Poisson and Ampère equations at the beginning of each numerical simulation, removes the initial transients of the simulation by imposing, at each position, the initial current expected from the cold plasma term of the electric field (so-called far-field term).

The net charge at any point in the simulation box is initialized to zero and the density of each species is initially uniform and equal everywhere in the simulation box.

$$n_e\,(x, t = 0) = n_i\,(x, t = 0) = n_0 \tag{A1}$$

$$n_{net}\,(x, t = 0) = n_i\,(x, t = 0) - n_e\,(x, t = 0) = 0 \tag{A2}$$

where x represents the position, t the time, n_e is the electron density, n_i is the ion density, n_0 is the unperturbed plasma density and n_{net} is the total charge density. The oscillating charges σ at the (infinite plane) emitting antennas are initialized to zero:

$$\sigma\,(t = 0) = 0. \tag{A3}$$

During the simulations, the oscillating charges at the antennas are imposed equal to $\bar{\sigma}\sin(\omega t)$, with $\bar{\sigma}$ its amplitude and ω the emission frequency. The electric field, computed from the initial net-charge, is zero everywhere in the simulation box:

$$E\,(x, t = 0) = 0 \tag{A4}$$

where E is the electric field. To ensure the consistency between the Poisson and Ampère equations at the beginning of each simulation, we initialize the current considering the current injected in the plasma at the emitting antenna and considering the time derivative of the initial electric field (Podesta, 2005) at each position in the simulated box.

The external current density injected from the emitting antenna in the plasma, at the beginning of the simulation, reads:

$$j_{ext}\,(t = 0) = \bar{\sigma}\omega \tag{A5}$$

where $\bar{\sigma}$ is the amplitude of the homogeneous charge per unit surface on the infinite charged plane. At each position, the expected current density, in the electrostatic 1D case, reads:

$$j_{tot}\,(t=0) = -\epsilon_0 \frac{\partial E}{\partial t} \tag{A6}$$

For emission frequencies close to the plasma frequency, the electric field reads (Podesta, 2005):

$$E = \frac{\bar{\sigma}\sin(t\omega)}{2\epsilon_0\left(1-\frac{\omega_p^2}{\omega^2}\right)}\mathrm{sgn}(x) \tag{A7}$$

where ω_p is the plasma frequency. The difference between the expected current density at each position and the current density sent in the plasma by the external antenna gives the initial current density we need to impose at each position in the simulation box. This current density is imposed via an offset on the velocity distribution functions with which we initialize the electrons, converting the initial Maxwellian distribution to a drifting Maxwellian. This velocity offset reads:

$$\frac{v_{offset}}{v_{the}} = \frac{\hat{\sigma}}{2}\frac{\hat{\omega}}{\frac{\omega^2}{\omega_p^2}-1} \tag{A8}$$

where v_{offset} is the velocity offset of the Maxwellian distributions of the electrons at initialization, v_{the} is the electron thermal velocity and $\hat{\sigma} = \sigma/\bar{\sigma}$ is the amplitude of the non-dimensional charge per unit surface imposed at the emitting antennas, with $\bar{\sigma}$ the planar charge distribution used to normalize the model.

This initialization minimizes the transients generated in the plasma when switching-on the emission at the electric antennas. This initialization is used in our study both for model A and model B.

Appendix B: Validation of the Model

In this appendix, we describe the validation of the two models (model A and model B) used in this study.

First, the numerical model is validated by comparing the simulated electric oscillations in the numerical box, at given distance from the emitting antenna and at given time after the beginning of the emission, against the electric oscillations expected analytically considering temporal and spatial Landau Damping of the emitted waves. These expected electric fluctuations are derived by solving the Vlasov-Poisson coupled equations as described, for example, in Krall and Thrivelpiece (1973), limiting the analysis to real frequencies and complex wavenumbers. A similar computation of the analytic expressions for this 1D-1 V case study is described in Podesta (2005). The validation of model A (resp. B) is illustrated in Panel a (resp. b) of Figure B1 as the comparison between the expected electric fluctuations (black line) and the simulated electric field oscillations (red line), computed for emission frequency $\omega = 1.1\omega_p$ at time $t = 100\omega_p^{-1}$ and in function of the emitting-receiving antennas distance. The emitted wave-packet propagates from the emitting antennas at group velocity and, along the distance it covers, the expected and simulated electric fluctuations agree. Note that limited differences are expected, since the analytic approximation is derived considering only the dominant pole and neglecting higher-order solutions (Podesta, 2005). The frequency-wavenumber couples used to obtain the analytic electric oscillations are computed using the linear Vlasov-Maxwell solver WHAMP (Roennmark, 1982), in the limit of an unmagnetized plasma. Second, we validate the MI spectra obtained numerically against spectra derived using the DSCD model (Béghin & Kolesnikova, 1998; Geiswiller et al., 2001; Wattieaux et al., 2019; Wattieaux et al., 2020) which is the reference numerical tool for the modeling of MI instrumental response in the case of electrostatic linear perturbations of the plasma. This model is typically used to validate MI experimental measurements because, at the state of the art, it is the only MI model capable of taking into account the presence of the satellite platform when deriving MI spectra. In contrast to our 1D model, the DSCD model supposes very long emission periods (e.g., MI emission starts at time $t = -\infty$) and neglects the transient (delay) time required by the wave-packet generated at the emitting antennas to cover the receiving-emitting antennas distance.

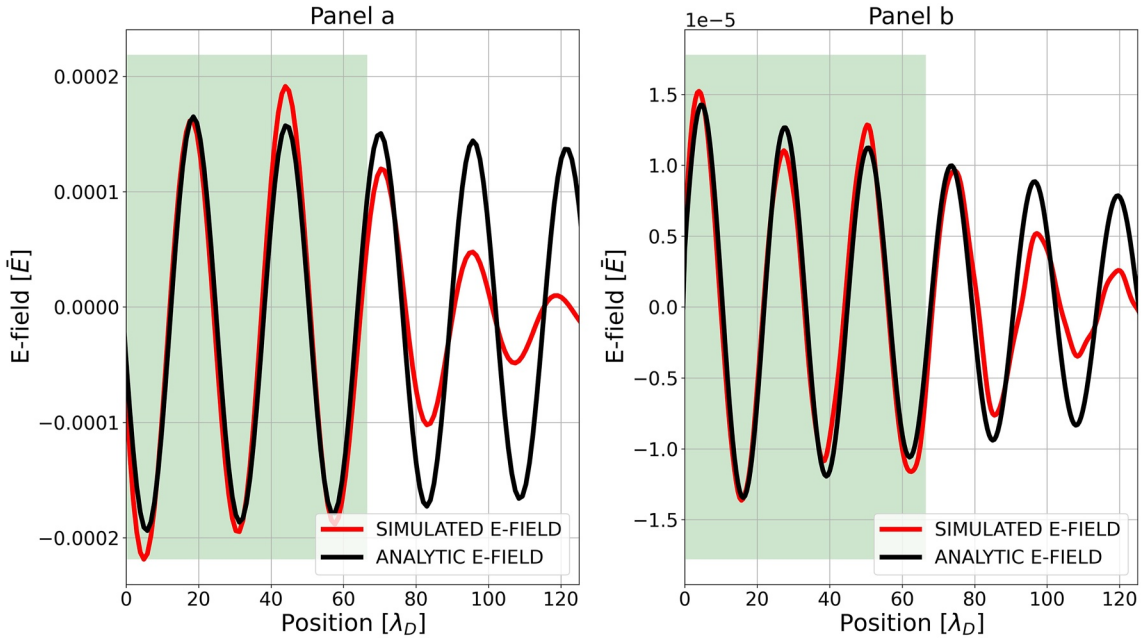

Figure B1. Validation of model A (panel A) and model B (panel b). Comparison between the electric fluctuations obtained numerically (red solid line) and those computed analytically (black solid line), in function of the emitting-receiving antennas distance, for the emission frequency $\omega = 1.1\omega_p$ and at time $t = 100\omega_p^{-1}$. At such time the emitted wave packet, propagating at group velocity $v_g = 0.67v_{the}$, has covered the distance $d = 67\lambda_D$ (green shaded area).

The comparison between spectra is performed for different emitting-receiving antennas distances and for antenna emission amplitudes corresponding to an electric-to-thermal energy ratio of 10^{-10}. The comparison is illustrated in Figure B2 for distances $d = 0.5\lambda_D$, $d = 5\lambda_D$, $d = 20\lambda_D$, and $d = 40\lambda_D$. On the one hand, for d smaller than $5\lambda_D$, the spectra disagree because of differences in the modeling of the emitting antennas between the two models. On the other hand, for d larger than $5\lambda_D$, the spectra agree. Therefore, to assess the diagnostic performance of MI experiments to finite emission amplitudes, we focus on emitting-receiving antennas distances larger than $5\lambda_D$ and neglect smaller distances.

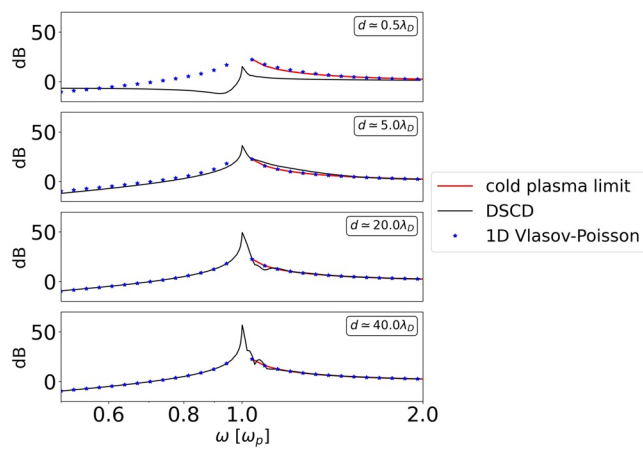

Figure B2. Comparison between spectra derived using our 1D Vlasov-Poisson model (blue points) and the DSCD model (black solid line). The red line represents the expected cold plasma response, valid for $\frac{\omega}{\omega_p} \gg 1$.

Appendix C: Model Parameters

In Table C1, for completeness and repeatability purposes, we show the parameters used for each numerical simulation.

Table C1

List of Numerical Simulation Settings Parameters for Investigating Non-Linear Perturbations of the Plasma: Total Length of the Simulation Box (X_{max}), Velocity Range for the Electron Distribution Function (V_e), Velocity Range for the Ion Distribution Function (V_i), Amount of Spatial Mesh Points (n_x), Amount of Velocity Mesh Points for Electrons (n_{ve}), Amount of Velocity Mesh Points for Ions (n_{vi}), Advancement Time Resolution of the Simulation (dt), Emission Frequency (ω), Oscillating Charges at the Antenna (σ), Ion-To-Electron Mass Ratio (m_i/m_e), Ion-To-Electron Temperature Ratio (T_i/T_e), and Electric-To-Thermal Energy Ratio ($E^2/(k_BT_e)$)

Name	M	$X_{\max}\,[\lambda_D]$	$V_{\max\ e}\,[v_{the}]$	$v_i\,[v_{thi}]$	n_x	n_{v_e}	n_{v_i}	$\mathrm{dt}\left[\omega_p^{-1}\right]$	$\omega\,[\omega_p]$	$\sigma\,[\bar{\sigma}]$	$\frac{m_i}{m_e}$	$\frac{T_i}{T_e}$	$\frac{E^2}{k_BT_e}$
LF_01	A	1,000	(−25,25)	(−25,25)	2,048	601	601	1e−3	0.5	1e−5	inf	0.1	1e−10
LF_02	A	1,000	(−25,25)	(−25,25)	2,048	601	601	1e−3	1.1	1e−5	inf	0.1	1e−8
LF_03	A	1,000	(−25,25)	(−25,25)	2,048	601	601	1e−3	2.0	1e−5	inf	0.1	1e−10
NF_01	A	1,000	(−25,25)	(−25,25)	2,048	601	601	1e−3	0.5	0.1	inf	0.1	0.01
NF_02	A	1,000	(−25,25)	(−25,25)	2,048	601	601	1e−3	1.1	0.1	inf	0.1	0.33
NF_03	A	1,000	(−25,25)	(−25,25)	2,048	601	601	1e−3	2.0	0.1	inf	0.1	0.01
NI_01	A	1,000	(−25,25)	(−25,25)	2,048	601	601	1e−3	0.5	0.1	100	0.1	0.01
NI_02	A	1,000	(−25,25)	(−25,25)	2,048	601	601	1e−3	1.1	0.1	100	0.1	0.33
NI_03	A	1,000	(−25,25)	(−25,25)	2,048	601	601	1e−3	2.0	0.1	100	0.1	0.01

Note. M represents the antennas configuration (model) used for these simulations.

In Tables C1 and C2 for completeness and repeatability purposes we show the parameters used for each numerical simulation. Table C1 (resp. Table C2) refers to the simulations supporting the discussion of Section 3 (resp. Section 4). LF (resp. SL) means Low Fixed (resp. Sweep Low) and indicates simulations used to investigate the plasma perturbations due to *single* fixed frequency (resp. sweep) emission(s) in the case of low amplitudes, associated to a linear plasma response. NI (resp. SI) means Non-linear Ions (resp. Sweep Ions) and simulate instead fixed frequency (resp. sweep) emissions in the case of moving ions with large emission amplitudes, associated to significant perturbations of the plasma. NF means Non-linear Fixed and indicates simulations supporting the discussion of Section 3.1, where we investigate plasma perturbations due to strong amplitude signals in the case of a fixed background of positive charges. MI sweep measurements are built using a number of different numerical runs with same numerical boxes but different emitted frequency. If one line is used to indicate in Table C2 each emitted frequency, the result would be a very long table with very diluted information. For simplicity purposes and to help the reader focus on the significant information of the table, we give instead the frequency resolution of the sweep measurement (last column of Table C2) which one can use to extrapolate the information regarding all emitted frequencies. Therefore, for each simulated MI sweep we only give two lines. One line corresponding to the first emitted frequency of the sweep and one corresponding to the last frequency of the sweep. For instance, SL_01 is the numerical simulation used to investigate the first frequency, $\omega_{SL,01} = 0.5\omega_p$, of one sweep measurement. SL_48 is the simulation investigating the last frequency, $\omega_{SL48} = 4.95\omega_p$, of the same measurement. The rest of the simulated frequencies of the sweep are obtained as $\omega_{n+1} = 1.05\omega_n$. We note that the LF simulations of Table C1 have not been used in the discussion of Section 3, but rather served us as reference during the analysis.

Table C2

List of Numerical Simulation Settings Parameters for Building MI Spectra: Total Length of the Simulation Box (X_{max}), Velocity Range for the Electron Distribution Function (V_e), Velocity Range for the Ion Distribution Function (V_i), Amount of Spatial Mesh Points (n_x), Amount of Velocity Mesh Points for Electrons (n_{ve}), Amount of Velocity Mesh Points for Ions (n_{vi}), Advancement Time Resolution of the Simulation (dt), Emission Frequency (ω), Oscillating Charges at the Antenna (σ), Ion-To-Electron Mass Ratio (m_i/m_e), Ion-To-Electron Temperature Ratio (T_i/T_e), and Frequency Sweep Resolution (ω_{n+1}/ω_n)

Name	M	$X_{\max}$ $[\lambda_D]$	$V_{\max\ e}$ $[v_{the}]$	v_i $[v_{thi}]$	n_x	n_{v_e}	n_{v_i}	dt $[\omega_p^{-1}]$	ω $[\omega_p]$	σ $[\bar{\sigma}]$	$\frac{m_i}{m_e}$	$\frac{T_i}{T_e}$	$\frac{\omega_{n+1}}{\omega_n}$
SL_01	B	4,000	(−25,25)	(−25,25)	8,192	601	601	1e−3	0.5	1e−5	100	0.1	1.05
SL_48	B	4,000	(−25,25)	(−25,25)	8,192	601	601	1e−3	4.95	1e−5	100	0.1	1.05
SI1_01	B	4,000	(−25,25)	(−25,25)	8,192	601	601	1e−3	0.77	0.1	100	0.1	1.05
SI1_14	B	4,000	(−25,25)	(−25,25)	8,192	601	601	1e−3	1.53	0.1	100	0.1	1.05
SI2_01	B	4,000	(−25,25)	(−25,25)	8,192	601	601	1e−3	0.77	0.31	100	0.1	1.05
SI2_14	B	4,000	(−25,25)	(−25,25)	8,192	601	601	1e−3	1.53	0.31	100	0.1	1.05
SI3_01	B	4,000	(−25,25)	(−25,25)	8,192	601	601	1e−3	0.77	0.6	100	0.1	1.05
SI3_14	B	4,000	(−25,25)	(−25,25)	8,192	601	601	1e−3	1.53	0.6	100	0.1	1.05
SI4_01	B	4,000	(−40,40)	(−25,25)	8,192	1,001	601	5e−4	0.77	1.0	100	0.1	1.05
SI4_14	B	4,000	(−40,40)	(−25,25)	8,192	1,001	601	5e−4	1.53	1.0	100	0.1	1.05

Note. M represents the antennas configuration (model) used for these simulations.

Data Availability Statement

Data sets for this research are available at Bucciantini (2022), together with a detailed explanation on how to use them. The model used to produce such data set is described in Section 2. It is based on the model implemented by Mangeney et al. (2002). The 1D-1 V Vlasov-Poisson version of the model, which corresponds to the one we use in our investigation, is described in Henri et al. (2010).

Acknowledgments

The work performed at LPC2E is supported by CNES APR. The Scientific colour map "lajolla" (Crameri, 2021) is used in this study to prevent visual distortion of the data and exclusion of readers with colour-vision deficiencies(Crameri et al., 2020). We acknowledge the use of the WHAMP software Roennmark (1982) for the validation of the model. We benefited from the computing resources provided by CaSciModOT. This work was granted access to the HPC/AI resources of TGCC under the allocation 2021-A0100412428 made by GENCI. L. B. was supported by funds from Région Centre Val de Loire (France).

References

Bahnsen, A., Jespersen, M., Ungstrup, E., Pottelette, R., Malingre, M., Decreau, P., et al. (1988). First VIKING results: High frequency waves. *Physica Scripta*, *37*(3), 469–474. https://doi.org/10.1088/0031-8949/37/3/032

Béghin, C. (1995). Series expansion of electrostatic potential radiated by a point source in isotropic Maxwellian plasma. *Radio Science*, *30*(2), 307–322. https://doi.org/10.1029/94RS03167

Béghin, C., & Debrie, R. (1972). Characteristics of the electric field far from and close to a radiating antenna around the lower hybrid resonance in the ionospheric plasma. *Journal of Plasma Physics*, *8*(3), 287–310. https://doi.org/10.1017/S0022377800007157

Béghin, C., Décréau, P. M. E., Pickett, J., Sundkvist, D., & Lefebvre, B. (2005). Modeling of cluster's electric antennas in space: Application to plasma diagnostics. *Radio Science*, *40*(6). https://doi.org/10.1029/2005RS003264

Béghin, C., Karczewski, J. F., Poirier, B., Debrie, R., & Masevich, N. (1982). The ARCAD-3 ISOPROBE experiment for high time resolution thermal plasma measurements. *Annales de Geophysique*, *38*(5), 615–629.

Béghin, C., & Kolesnikova, E. (1998). Surface-charge distribution approach for modeling of quasi-static electric antennas in isotropic thermal plasma. *Radio Science*, *33*(3), 503–516. https://doi.org/10.1029/97RS03588

Brunetti, M., Califano, F., & Pegoraro, F. (2000). Asymptotic evolution of nonlinear Landau damping. *Physical Review E - Statistical Physics, Plasmas, Fluids, and Related Interdisciplinary Topics*, *62*(3), 4109–4114. https://doi.org/10.1103/PhysRevE.62.4109

Bucciantini, L. (2022). *1D-1V Vlasov-Poisson simulations of mutual impedance experiments for strong antenna emission amplitudes*. Zenodo. https://doi.org/10.5281/zenodo.7149358

Buckley, R. (1968). Radio frequency properties of a plane grid capacitor immersed in a hot collision-free plasma. *Journal of Plasma Physics*, *2*(3), 339–351. https://doi.org/10.1017/S0022377800003871

Califano, F., Galeotti, L., & Briand, C. (2007). Electrostatic coherent structures: The role of the ions dynamics. *Physics of Plasmas*, *14*(5), 052306. https://doi.org/10.1063/1.2724807

Califano, F., & Lontano, M. (1999). Vlasov-Poisson simulations of strong wave-plasma interaction in conditions of relevance for radio frequency plasma heating. *Physical Review Letters*, *83*(1), 96–99. https://doi.org/10.1103/PhysRevLett.83.96

Chasseriaux, J., Debrie, R., & Renard, C. (1972). Electron density and temperature measurements in the lower ionosphere as deduced from the warm plasma theory of the h.f. quadrupole probe. *Journal of Plasma Physics*, *8*(2), 231–253. https://doi.org/10.1017/S0022377800007108

Chasseriaux, J. M. (1972). Potential set up by a point charge oscillating in magnitude in an inhomogeneous plasma. *Plasma Physics*, *14*(8), 763–781. https://doi.org/10.1088/0032-1028/14/8/002

Chassériaux, J. M. (1974). Excitation of the plasma and upper hybrid resonances in a warm magnetoplasma by an alternating electric dipole. *Journal of Plasma Physics*, *11*(2), 225–252. https://doi.org/10.1017/S0022377800024624

Crameri, F. (2021). *Scientific colour maps*. Zenodo. https://doi.org/10.5281/zenodo.5501399

Crameri, F., Shephard, G. E., & Heron, P. J. (2020). The misuse of colour in science communication. *Nature Communications*, *11*(1), 5444. https://doi.org/10.1038/s41467-020-19160-7

Décréau, P. M. E., Beghin, C., & Parrot, M. (1978). Electron density and temperature, as measured by the mutual impedance experiment on board GEOS-1 (Article published in the special issues: Advances in Magnetospheric Physics with GEOS- 1 and ISEE - 1 and 2.). *Space Science Reviews*, *22*(5), 581–595. https://doi.org/10.1007/BF00223942

Décréau, P. M. E., Hamelin, M., Massif, R., de Feraudy, H., & Pawela, E. (1987). Plasma probing by active wave experiments on the Viking satellite. *Annales Geophysicae*, *5*, 181–185.

Dysthe, K. B., & Franklin, R. (1970). Non-linear interactions of coherent electrostatic plasma waves. *Plasma Physics*, *12*(9), 705–721. https://doi.org/10.1088/0032-1028/12/9/005

Eriksson, A. I., Engelhardt, I. A. D., André, M., Boström, R., Edberg, N. J. T., Johansson, F. L., et al. (2017). Cold and warm electrons at comet 67p/churyumov-gerasimenko. *A&A*, *605*, A15. https://doi.org/10.1051/0004-6361/201630159

Geiswiller, J., Béghin, C., Kolesnikova, E., Lagoutte, D., Michau, J. L., & Trotignon, J. G. (2001). Rosetta spacecraft influence on the mutual impedance probe frequency response in the long Debye length mode. *Planetary and Space Science*, *49*(6), 633–644. https://doi.org/10.1016/S0032-0633(00)00173-2

Gilet, N., Henri, P., Wattieaux, G., Cilibrasi, M., & Béghin, C. (2017). Electrostatic potential radiated by a pulsating charge in a two-electron temperature plasma. *Radio Science*, *52*(11), 1432–1448. https://doi.org/10.1002/2017RS006294

Grard, R. (1969). Coupling between two electric aerials in a warm plasma. *Alta Frequency*, *38*, 97–101.

Grard, R. (1997). Influence of suprathermal electrons upon the transfer impedance of a quadrupolar probe in a plasma. *Radio Science*, *32*(3), 1091–1100. https://doi.org/10.1029/97RS00254

Harvey, C. C., Etcheto, J., & Mangeney, A. (1979). Early results from the isee electron density experiment. In K. Knott, A. Durney, & K. Ogilvie (Eds.), *Advances in magnetospheric physics with GEOS-1 and ISEE* (pp. 533–552). Springer Netherlands. https://doi.org/10.1007/978-94-009-9527-7_34

Henri, P., Califano, F., Briand, C., & Mangeney, A. (2010). Vlasov-Poisson simulations of electrostatic parametric instability for localized Langmuir wave packets in the solar wind. *Journal of Geophysical Research*, *115*(A6), A06106. https://doi.org/10.1029/2009JA014969

Henri, P., Califano, F., Briand, C., & Mangeney, A. (2011). Low-energy Langmuir cavitons: Asymptotic limit of weak turbulence. *EPL (Europhysics Letters)*, *96*(5), 55004. https://doi.org/10.1209/0295-5075/96/55004

Henri, P., Vallières, X., Hajra, R., Goetz, C., Richter, I., Glassmeier, K.-H., et al. (2017). Diamagnetic region(s): Structure of the unmagnetized plasma around comet 67p/cg. *Monthly Notices of the Royal Astronomical Society*, *469*(Suppl_2), S372–S379. https://doi.org/10.1093/mnras/stx1540

Kasaba, Y., Kojima, H., Moncuquet, M., Wahlund, J., Yagitani, S., Sahraoui, F., et al. (2020). Plasma wave investigation (PWI) aboard Bepi-Colombo Mio on the trip to the first measurement of electric fields, electromagnetic waves, and radio waves around mercury. *Space Science Reviews*, *216*(65), 65. https://doi.org/10.1007/s11214-020-00692-9

Krall, N., & Thrivelpiece, A. (1973). *Principles of plasma physics*. McGraw-Hill.

Mangeney, A., Califano, F., Cavazzoni, C., & Travnicek, P. (2002). A numerical scheme for the integration of the Vlasov-Maxwell system of equations. *Journal of Computational Physics*, *179*(2), 495–538. https://doi.org/10.1006/jcph.2002.7071

Odelstad, E., Eriksson, A. I., André, M., Graham, D. B., Karlsson, T., Vaivads, A., et al. (2020). Plasma density and magnetic field fluctuations in the ion gyro-frequency range near the diamagnetic cavity of comet 67P. *Journal of Geophysical Research: Space Physics*, *125*(12). https://doi.org/10.1029/2020JA028192

O'Neil, T. (1965). Collisionless damping of nonlinear plasma oscillations. *The Physics of Fluids*, *8*(12), 2255–2262. https://doi.org/10.1063/1.1761193

Osherovich, V. A., Benson, R. F., Fainberg, J., Stone, R. G., & MacDowall, R. J. (1993). Sounder stimulated d_n resonances in Jupiter's io plasma torus. *Journal of Geophysical Research*, *98*(E10), 18751–18756. https://doi.org/10.1029/93JE01481

Podesta, J. J. (2005). Spatial Landau damping in plasmas with three-dimensional k distributions. *Physics of Plasmas*, *12*(5), 052101. https://doi.org/10.1063/1.188547

Pottelette, R., Rooy, B., & Fiala, V. (1975). Theory of the mutual impedance of two small dipoles in a warm isotropic plasma. *Journal of Plasma Physics*, *14*(2), 209–243. https://doi.org/10.1017/S0022377800009533

Pottelette, R., & Storey, L. R. O. (1981). Active and passive methods for the study of non-equilibrium plasmas using electrostatic waves. *Journal of Plasma Physics*, *25*(2), 323–350. https://doi.org/10.1017/S0022377800023151

Roennmark, K. (1982). *Waves in Homogeneous, Anisotropic Multicomponent Plasmas*. WHAMP.

Rooy, B., Feix, M. R., & Storey, L. R. O. (1972). Theory of a quadripolar probe for a hot isotropic plasma. *Plasma Physics*, *14*(3), 275–300. https://doi.org/10.1088/0032-1028/14/3/005

Snodgrass, C., & Jones, G. H. (2019). The European space agency's comet interceptor lies in wait. *Nature Communications*, *10*(5418), 5418. https://doi.org/10.1038/s41467-019-13470-1

Storey, L., Aubry, L., & Meyer, P. (1969). Mutual impedance techniques for space plasma measurements. *Measurement techniques in space plasmas - Fields Geophysical Monograph Series*, *103*, 155–160. https://doi.org/10.1029/GM103p0155

Tkachenko, A., Krasnoselskikh, V., & Voshchepynets, A. (2021). Harmonic radio emission in randomly inhomogeneous plasma. *The Astrophysical Journal*, *908*(2), 126. https://doi.org/10.3847/1538-4357/abd2bd

Trotignon, J., Béghin, C., Lagoutte, D., Michau, J., Matsumoto, H., Kojima, H., et al. (2006). Active measurement of the thermal electron density and temperature on the mercury magnetospheric orbiter of the bepicolombo mission. *Advances in Space Research*, *38*(4), 686–692. https://doi.org/10.1016/j.asr.2006.03.031

Trotignon, J., Etcheto, J., & Thouvenin, J. (1986). Automatic determination of the electron density measured by the relaxation sounder on board ISEE 1. *Journal of Geophysical Research*, *91*(A4), 4302. https://doi.org/10.1029/JA091iA04p04302

Trotignon, J., Michau, J. L., Lagoutte, D., Chabassiere, M., Chalumeau, G., Colin, F., et al. (2007). RPC-MIP: The mutual impedance probe of the Rosetta plasma Consortium. *Space Science Reviews*, *128*(1–4), 713–728. https://doi.org/10.1007/s11214-006-9005-1

Trotignon, J., Rauch, J., Décréu, P., Canu, P., & Lemaire, J. (2003). Active and passive plasma wave investigations in the earth's environment: The cluster/whisper experiment. *Advances in Space Research*, *31*(5), 1449–1454. https://doi.org/10.1016/S0273-1177(02)00959-6

Trotignon, J. G., Décréau, P. M. E., Rauch, J. L., Vallières, X., Rochel, A., Kougblénou, S., et al. (2010). The whisper relaxation sounder and the cluster active archive.

Wattieaux, G., Gilet, N., Henri, P., Vallières, X., & Bucciantini, L. (2019). Rpc-mip observations at comet 67p/churyumov-gerasimenko explained by a model including a sheath and two populations of electrons. *A&A*, *630*, A41. https://doi.org/10.1051/0004-6361/201834872

Wattieaux, G., Henri, P., Gilet, N., Vallières, X., & Deca, J. (2020). Plasma characterization at comet 67p between 2 and 4 au from the sun with the rpc-mip instrument. *A&A*, *638*, A124. https://doi.org/10.1051/0004-6361/202037571

Youssef, E. (1996). ECSS - European Cooperation for Space Standardization. In *Space programs and technologies conference*. https://doi.org/10.2514/6.1996-4305

Zakharov, V. E., & Karpman, V. I. (1963). On the nonlinear theory of the damping of plasma waves. *Soviet Journal of Experimental and Theoretical Physics*, *16*, 351.